

# High-resolution mm and cm study of the obscured LIRG NGC 4418<sup>\*</sup>

## A compact obscured nucleus fed by in-falling gas?

F. Costagliola<sup>1,2</sup>, S. Aalto<sup>2</sup>, K. Sakamoto<sup>3</sup>, S. Martín<sup>4</sup>, R. Beswick<sup>5</sup>, S. Müller<sup>2</sup>, and H.-R. Klöckner<sup>6,7</sup>

<sup>1</sup> Instituto de Astrofísica de Andalucía, Glorieta de la Astronomía, s/n, 18008 Granada, Spain  
e-mail: costagli@iaa.es

<sup>2</sup> Chalmers University of Technology, Onsala Space Observatory, 439 92 Onsala, Sweden

<sup>3</sup> Academia Sinica, Institute of Astronomy and Astrophysics, PO Box 23-141, 10617 Taipei, Taiwan

<sup>4</sup> European Southern Observatory, Alonso de Córdova 3107, Vitacura, Casilla 19001, Santiago 19, Chile

<sup>5</sup> Jodrell Bank Centre for Astrophysics, Alan Turing Building, School of Physics and Astronomy, The University of Manchester, Manchester M13 9PL, UK

<sup>6</sup> University of Oxford, Denys Wilkinson Building, Oxford OX1 3RH, UK

<sup>7</sup> Max-Planck-Institut für Radioastronomie, Auf dem Hügel 69, 53121 Bonn, Germany

Received 25 October 2012 / Accepted 10 June 2013

### ABSTRACT

**Context.** Understanding the nature of the power-source in luminous infrared galaxies (LIRG) is difficult due to their extreme obscuration. Observations at radio and mm wavelengths can penetrate large columns of dust and gas and provide unique insights into the properties of the compact obscured nuclei of LIRGs.

**Aims.** The aim of this study is to constrain the dynamics, structure, and feeding of the compact nucleus of NGC 4418, and to reveal the nature of the main hidden power-source: starburst or active galactic nucleus (AGN).

**Methods.** We obtained high spatial resolution observations of NGC 4418 at 1.4 and 5 GHz with MERLIN, and at 230 and 270 GHz with the SMA in very extended configuration. We used the continuum morphology and flux density to estimate the size of the emitting region, the star formation rate, and the dust temperature. Emission lines were used to study kinematics through position-velocity diagrams. Molecular emission was studied with population diagrams and by fitting a local thermal equilibrium (LTE) synthetic spectrum.

**Results.** We detect bright 1-mm-line emission from CO, HC<sub>3</sub>N, HNC, and C<sup>34</sup>S and 1.4 GHz absorption from HI. The CO 2–1 emission and HI absorption can be fit by two velocity components at 2090 and 2180 km s<sup>-1</sup>. We detect vibrationally excited HC<sub>3</sub>N and HNC, with  $T_{\text{vib}} \sim 300$  K. Molecular excitation is consistent with a layered temperature structure, with three main components at 80, 160, and 300 K. For the hot component we estimate a source size of less than 5 pc. The nuclear molecular gas surface density of  $10^4 M_{\odot} \text{pc}^{-2}$  is extremely high and similar to that found in the ultra-luminous infrared galaxy (ULIRG) Arp220.

**Conclusions.** Our observations confirm the presence of a molecular and atomic in-flow, previously suggested by *Herschel* observations, which is feeding the activity in the center of NGC 4418. Molecular excitation confirms the presence of a very compact, hot dusty core. If a starburst is responsible for the observed IR flux, this has to be at least as extreme as the one in the ULIRG Arp 220, with an age of 3–10 Myr and a star formation rate  $>10 M_{\odot} \text{yr}^{-1}$ . If an AGN is present, it must be extremely Compton-thick.

**Key words.** galaxies: starburst – galaxies: active – galaxies: individual: NGC 4418 – galaxies: kinematics and dynamics – galaxies: ISM

## 1. Introduction

Luminous infrared galaxies (LIRG) radiate most of their energy as thermal dust emission in the infrared (IR) and constitute the dominant population among the most luminous extragalactic objects (e.g., Sanders & Mirabel 1996). Recent observations (Spoon et al. 2007; Aalto et al. 2007b; Costagliola et al. 2011) suggest that they may play a crucial role in galaxy evolution, representing the early obscured stages of starburst galaxies and active galactic nuclei (AGN).

The central regions of LIRGs are deeply enshrouded in large columns of gas and dust, which preclude direct investigation in the optical and IR. Observations at radio and mm/sub-mm wavelengths can penetrate these large amounts of obscuring material and provide unique insight into the properties of LIRGs. The

study of molecular line emission has proven to be a key player in this field by providing valuable information on the physical conditions of the gas, its chemistry, and dynamics. In a 3-mm-line survey with the IRAM EMIR broadband receiver (Costagliola et al. 2011) we found a small sample of HC<sub>3</sub>N-luminous and HCO<sup>+</sup>-faint galaxies. These objects have compact (<100 pc) obscured ( $A_{\text{V}} > 100 \text{ Mag}$ ) nuclei, characterized by deep silicate absorption in the mid-IR and rich molecular spectra, which cannot be explained by standard chemical models (e.g., Spaans & Meijerink 2004; Baan et al. 2008; Costagliola et al. 2011).

The peculiar spectral properties of compact obscure nuclei (CON) resemble to some degree those of Galactic hot cores and may be tracing the early, dust-enshrouded stages of nuclear activity. Very long baseline interferometry (VLBI) observations at radio wavelengths have revealed that the IR emission from LIRGs can be powered by both starburst and AGN activity (e.g., Pérez-Torres et al. 2009; Batejat et al. 2011). LIRGs can have

\* Appendix A is only available in electronic form at <http://www.aanda.org>

star formation rates (SFR) 10 to 100 times greater than what is observed in the Milky Way, and very high gas surface densities, which resemble the properties of star-forming sites in high-redshift submillimeter galaxies (SMGs; e.g. Swinbank et al. 2011). Whether the high SFR is due to the extreme gas surface densities (e.g., Kennicutt 1998) or to an increased star formation efficiency in high-pressure environments (e.g., Elmegreen & Efremov 1997) is still a matter of debate. Compact obscured nuclei are ideal laboratories for studying chemistry, molecular excitation, and star formation in extreme interstellar medium (ISM) conditions.

### 1.1. NGC 4418: The prototypical compact obscured nucleus

The LIRG NGC 4418 ( $L_{\text{IR}} = 10^{11} L_{\odot}$ ) has the optical morphology of an early-type spiral and was first detected as a bright source by the IRAS satellite. Lying at  $D = 34$  Mpc, the galaxy is part of an interacting pair, with the companion being an irregular blue galaxy roughly two arc-minutes (16 kpc) to the southeast.

The optical spectrum of NGC 4418 has been described by Roche et al. (1986) as unremarkable, with only faint emission from S[II] and  $H_{\alpha}$  on a strong continuum, and it does not betray the presence of the bright IR source. This is explained by mid-IR observations (Spoon et al. 2001; Roche et al. 1986), which show a deep silicate absorption at  $10 \mu\text{m}$ , one of the deepest ever observed in an external galaxy, corresponding to roughly 100 mag of visual extinction. Whatever is powering the strong IR flux of NGC 4418, it must be hidden behind a thick layer of dust, which makes it undetectable at optical wavelengths.

The high IR luminosity requires a compact starburst or an AGN to heat up a large column of dust. However, because of the high obscuration, the direct investigation of the nuclear region is a challenging task, and the nature of the energy source is still unclear. Observations with the *Chandra* X-ray satellite by Maiolino et al. (2003) show a flat hard X-ray spectrum, which would be an indication of a Compton-thick AGN, but the photon statistics is too limited to be conclusive. The absence of a clear X-ray signature may imply either that the galaxy is powered by star formation alone, or that the obscuring column is so high that most of the X-ray emission cannot escape its nuclear region.

Additional evidence of nuclear activity in NGC 4418 comes from near- and mid-IR observations. High-resolution HST near-IR and Keck mid-IR images by Evans et al. (2003) show that the galaxy has a 100–200 pc optically thick core, with an high IR surface brightness. The observed spectral energy distribution implies a dust temperature of 85 K, which, when compared with the total IR flux, implies the presence of an optically thick source of no more than 70 pc across. The existence of a compact source is confirmed also by observations of vibrationally excited  $\text{HC}_3\text{N}$  (Costagliola & Aalto 2010) and HCN (Sakamoto et al. 2010), which reveal dust temperatures of about 200–500 K, and a source size of less than 10 pc.

In a recent study Sakamoto et al. (2013) have used SMA observations at 860 and  $450 \mu\text{m}$  to directly probe the nucleus of NGC 4418 at subarcsecond resolution. This study confirms the existence of a  $\sim 20$  pc ( $0''.1$ ) hot dusty core, with a bolometric luminosity of about  $10^{11} L_{\odot}$ , which accounts for most of the galaxy luminosity. The high luminosity-to-mass ratio ( $L/M \simeq 500 L_{\odot} M_{\odot}^{-1}$ ) and luminosity surface density ( $10^{8.5 \pm 0.5} L_{\odot} \text{pc}^{-2}$ ) are consistent with a Compton-thick AGN to be the main luminosity source. Alternatively, an extreme ( $SFR \simeq 100 M_{\odot} \text{yr}^{-1}$ ), young ( $\leq 5$  Myr), compact starburst could also reproduce the properties of the inner core. By comparing SDSS optical images in the  $i'$ ,  $z'$ ,  $g'$ ,  $r'$  filters, a reddening feature was found

perpendicular to the major axis of the galaxy, which is interpreted as an outflow cone emanating from the nucleus.

NGC 4418 was first shown to have a rich molecular chemistry by Aalto et al. (2007a) and the large abundance of  $\text{HC}_3\text{N}$  ( $> 10^{-8}$ , Costagliola & Aalto 2010) is not obviously consistent with the X-ray-dominated chemistry expected in an AGN scenario (Meijerink et al. 2007). Together with a low  $\text{HCO}^+/\text{HCN}$   $J = 1-0$  line ratio, bright  $\text{HC}_3\text{N}$  is instead reminiscent of line emission toward Galactic hot-cores, i.e., regions of dense, warm, shielded gas around young stars. This has led some authors to propose that NGC 4418 may be a very young starburst, where the star-forming regions are still embedded in large amounts of dust (Aalto et al. 2007a; Costagliola et al. 2011). This scenario of a nascent starburst would be consistent with the galaxy being radio-deficient (Roussel et al. 2003). However, this picture is complicated by the possibility of a buried AGN, the required extreme properties of a buried starburst, and by recent chemical model developments suggesting that substantial  $\text{HC}_3\text{N}$  abundances may occur near AGNs (Harada et al. 2010).

Recent *Herschel* PACS observations (González-Alfonso et al. 2012) reveal the presence of a compact (5 pc), hot (350 K) core and redshifted OH absorption, which is interpreted as the signature of a molecular in-flow. These observations confirm previous estimates of the properties of the compact core (e.g., Costagliola & Aalto 2010), and suggest that a gas in-flow may be feeding the central engine. However, both single-dish and satellite observations lack the spatial resolution needed to directly probe the inner 100 pc and are thus highly model-dependent. The high angular resolution observations obtained with the MERLIN VLBI network presented here, and the Submillimeter Array (SMA) observations presented here and in the companion paper (Sakamoto et al. 2013), allow us to investigate the properties of the nuclear core with unprecedented accuracy.

## 2. Observations

### 2.1. MERLIN

NGC 4418 was observed with MERLIN<sup>1</sup>, including the 76-m *Lovell* Telescope, on 30/31 May 2005. The total duration of the observations was 12.4 h, including 7.8 h on-source observation of NGC 4418. Throughout the observing run, observations of NGC 4418 were regularly interspersed with scans on the nearby phase-reference calibration source 1216-010. A single scan of 3C 286 was used as the primary flux density calibrator and the bright point source calibrator 0552+398 was used for secondary flux density calibration and to derive bandpass solutions. The two hands of circular polarization were recorded over a total bandwidth of 4 MHz, centered on the redshifted frequency of HI (1410.165 MHz). The total bandwidth of the observations was correlated into 128 channels with width of 31.25 kHz equating to a velocity resolution of  $6.5 \text{ km s}^{-1}$ . Initial editing and calibration was performed at Jodrell Bank Observatory using the local MERLIN dprogs software before the data were exported to fits. Further calibration, including flux density, bandpass and phase-reference calibration were performed using the MERLIN pipeline, following standard procedures.

In addition to these MERLIN 1.4 GHz spectral line data, 5 GHz continuum data were extracted from the MERLIN archive. These data were observed on 3 June 2001 as part of

<sup>1</sup> MERLIN is a national facility operated by The University of Manchester on behalf of the Science and Technology Facilities Council (STFC).

**Table 1.** General properties of NGC 4418 assumed in the text.

Properties of NGC 4418	
Phase center (RA, Dec, J2000) <sup>1</sup>	12:26:54.611, -00:52:39.42
Distance <sup>2</sup>	34 ± 2 Mpc
Scale at Hubble flow distance <sup>2</sup>	165 pc/arcsec
Systemic velocity (LSR) <sup>3</sup>	2090 km s <sup>-1</sup>
IR luminosity (40–120 μm) <sup>4</sup>	10 <sup>10.63</sup> L <sub>⊙</sub>
IR luminosity (8–1000 μm) <sup>5</sup>	10 <sup>11.1</sup> L <sub>⊙</sub>
Classification <sup>2</sup>	LIRG, Seyfert 2

**Notes.** <sup>(1)</sup> Common phase center of all observations (position of the CO 2–1 intensity peak). <sup>(2)</sup> From the NASA/IPAC Extragalactic Database (NED): <http://ned.ipac.caltech.edu/>. <sup>(3)</sup> From HNC kinematics in Sakamoto et al. (2013). <sup>(4)</sup> From Baan & Klöckner (2006). <sup>(5)</sup> From IRAS flux in Sanders et al. (2003).

a combined MERLIN and EVN experiment. In total the observation lasted 7.8 h, with an on-source integration of 2.8 h on NGC 4418. Regular observations of the two phase-reference calibrators J1232-0224 and J1229+0203 were made throughout the run and a single 20 min scan of 3C 286 was used for flux density calibration. Observations of J0555+3948 and OQ208 were used to derive secondary flux calibration and band-pass. Six MERLIN telescopes (not including Lovell Telescope) were used, with the data correlated into 16 1-MHz-wide channels in all four Stokes. These continuum data were initially edited and calibrated using local MERLIN software before they were exported to fits for further analysis.

The calibrated data were imaged, cleaned, and analyzed with the GILDAS/MAPPING<sup>2</sup> data reduction package. To easily compare the different observations, a common phase center was set at  $\alpha_{J2000} = 12:26:54.611$  and  $\delta_{J2000} = -00:52:39.42$ , corresponding to the position of the peak of the CO 2–1 integrated intensity (see Sect. 4.1.1 and Table 1). The MERLIN observations were deconvolved using a Clark clean algorithm with uniform weighting, resulting in a beam size of 0′.35 × 0′.16 and position angle (PA) of 23° at 1.4 GHz, and a beam size of 0′.13 × 0′.04 with PA 19° at 5 GHz. The deconvolved spectral data cube at 1.4 GHz was smoothed to a velocity resolution of 20 km s<sup>-1</sup>. The spatial resolution of our observations is roughly 40 and 15 pc for observations at 1.4 GHz and 5 GHz, respectively.

## 2.2. SMA

Observations were carried out on February 24 and 27 2010 with the SMA<sup>3</sup> on Mauna Kea, Hawaii. All eight array antennas were available and placed in the very extended configuration, with baselines ranging between 120–500 m. Observations consisted of two tracks where the SIS receivers were tuned at the rest frequencies of 230.537 GHz and 271.981 GHz in the lower side-band.

The phase-reference center of the observations was  $\alpha_{J2000} = 12:26:54.60$  and  $\delta_{J2000} = -00:52:39.0$ . Gain calibration was checked every 15 min by observing the nearby (~3°) quasar 3C 273. Bandpass calibration was derived from the spectrum of J0854+201, while absolute flux calibration was performed on

<sup>2</sup> <http://www.iram.fr/TRAMFR/GILDAS>

<sup>3</sup> The Submillimeter Array (SMA) is a joint project between the Smithsonian Astrophysical Observatory and the Academia Sinica Institute of Astronomy and Astrophysics and is funded by the Smithsonian Institution and the Academia Sinica.

Mars, Titan, and Ceres. Average zenith opacities at 225 GHz during the observations were 0.07 and 0.09, corresponding to a precipitable water vapor (PWV) of ~1 and 2 mm, respectively. Data calibration and reduction was performed using the MIRIDL package.

The calibrated data were deconvolved using a Clark CLEAN algorithm with uniform weighting, resulting in a beam size of 0′.49 × 0′.38 and 0′.41 × 0′.33 at 230 and 270 GHz, respectively, and a position angle of 60°. The resulting deconvolved spectral data cubes were smoothed to a common velocity resolution of 20 km s<sup>-1</sup>. The spatial resolution of our observations at 1 mm is roughly 50 pc.

## 3. Results

### 3.1. 1.4 GHz and 5 GHz continuum

The maps of continuum emission are shown in Fig. 1, while the integrated intensity maps of the detected lines can be found in Fig. 2. Source sizes were derived for the continuum and spectral line emission via fitting elliptical Gaussians in the  $uv$ -domain, with the MAPPING routine UV\_FITS, and were compared with circle-averaged visibility profiles (see Fig. A.1).

The radio continuum in NGC 4418 was detected in both MERLIN bands, with integrated total flux densities of 38 and 34 mJy at 1.4 and 5 GHz, respectively. Our data agree with previous observations with the VLA by Baan & Klöckner (2006). These authors detected the same total flux density in a similar beam, but did not discuss the structure of the emission, assuming the source to be unresolved. According to the  $uv$ -fitting and circle-averaged profiles in our data, the emission appears to be spatially resolved, with source sizes of 0′.5 at 1.4 GHz and 0′.15 at 5 GHz, corresponding to a linear extent of 80 and 25 pc (see Fig. 1, A.1).

At 1.4 and 5 GHz, filaments departing from the central peak are detected at the 3 $\sigma$  level. These filaments have an orientation roughly perpendicular to the major axis of the galaxy (from 2MASS, PA  $\approx$  60°, Skrutskie et al. 2006) and extend to 100 and 30 pc out of the projected galactic plane at 1.4 and 5 GHz, respectively. This detection, however, still needs to be considered tentative, because of the poor beam quality of the MERLIN interferometer at low declinations, and has yet to be confirmed.

### 3.2. HI absorption

The 21-cm atomic hydrogen line is clearly detected in absorption toward the nucleus of NCG 4418. The HI absorption is spatially resolved, covering the whole extent of the 1.4 GHz continuum. We estimate a lower limit for the angular diameter of the absorbing HI gas of 0′.5, corresponding to a linear size of 70 pc at the galaxy distance. The maximum of the absorption is slightly displaced from the phase center and from the maximum of the 1.4 GHz continuum, with offsets +0′.05 and -0′.05 in RA and Dec, respectively.

In Fig. 3 we show the first- and second-moment maps of HI, together with position-velocity (PV) diagrams along PA = 45° and PA = 135°. As projection angles we chose the major and minor axis of the integrated CO 2–1 emission (see Figs. 2 and 3). The velocity-centroid map and the PV diagrams show no clear sign of rotation, but a velocity gradient of roughly 70 km s<sup>-1</sup> pc<sup>-1</sup> is marginally detected along the major axis of the galaxy.

The continuum-subtracted HI spectrum extracted from the central beam is shown in Fig. 5c. The line profile appears skewed, with a marked blue excess extending to local standard

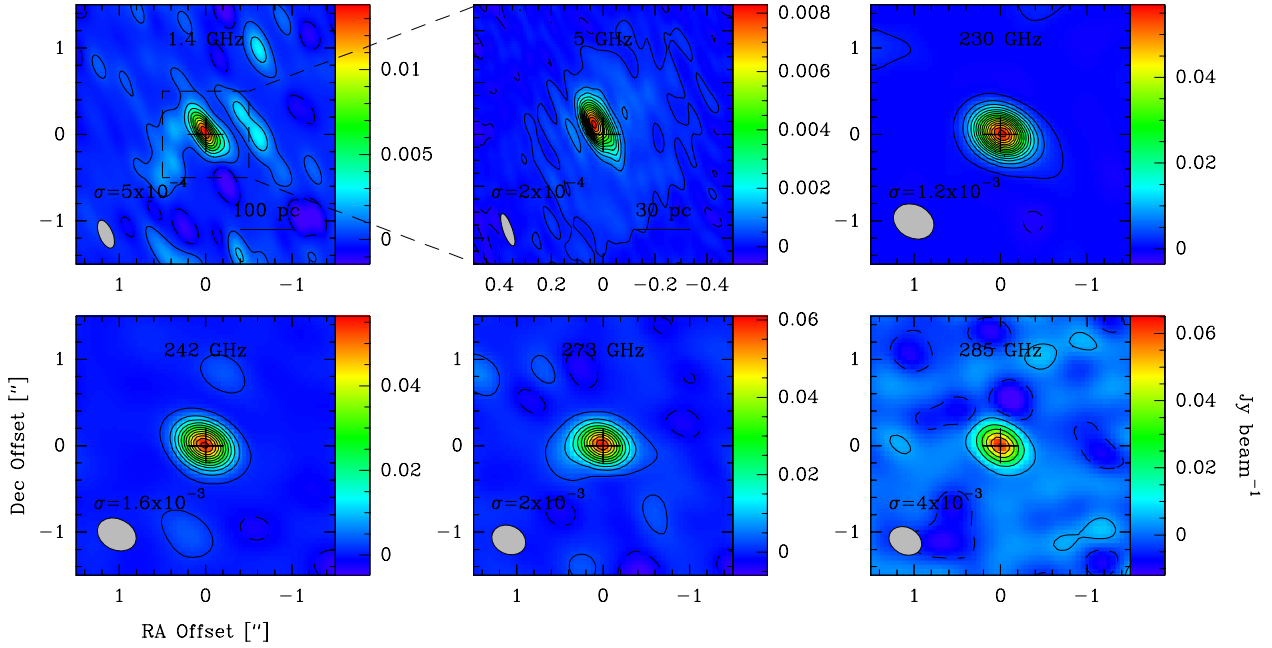


**Fig. 1.** Maps of continuum emission for MERLIN and SMA observations in NGC 4418. Contours are drawn every  $3\sigma$ , starting at  $1\sigma$ . Negative contours are drawn as dashed lines. Position offsets are given relative to the phase center reported in Table 1.

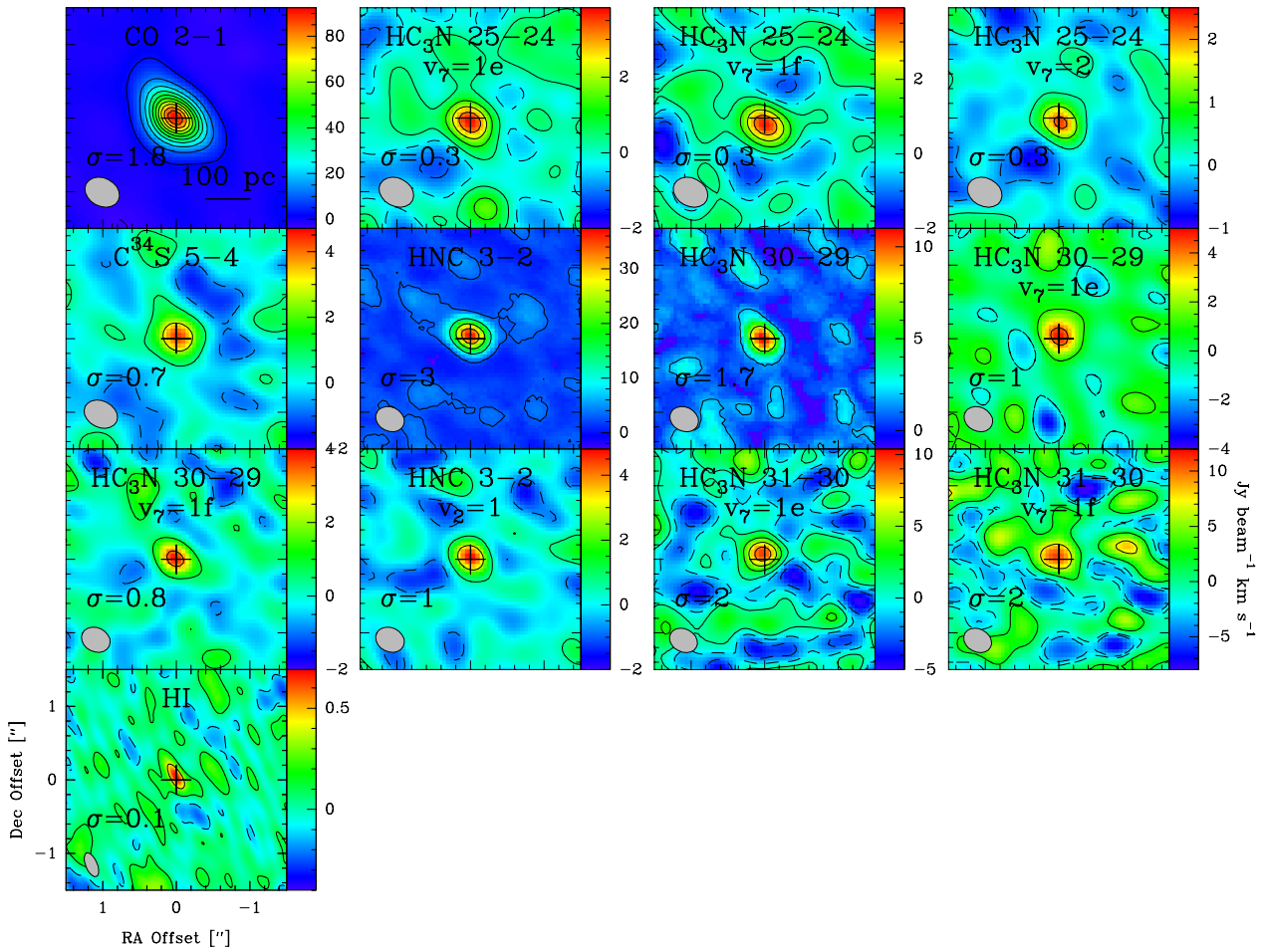


**Fig. 2.** Continuum-subtracted integrated intensity maps of all lines detected in the SMA and MERLIN bands. Contours are drawn every  $5\sigma$  for CO, and every  $3\sigma$  for the other lines, starting at  $1\sigma$ . Negative contours are drawn as dashed lines. For convenience, the intensity scale for HI absorption has been inverted. Position offsets are relative to the phase center reported in Table 1.

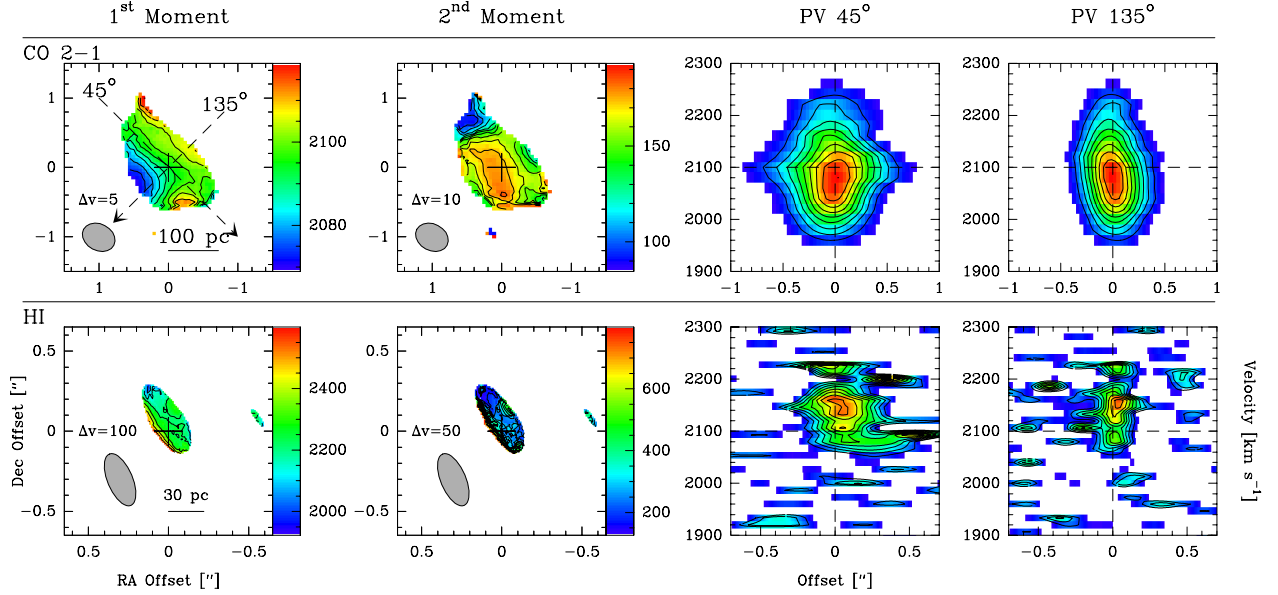


**Fig. 3.** Kinematics of CO 2–1 emission and HI absorption. The first and second moments of the deconvolved data-cubes are shown, together with position-velocity diagrams along the major ( $45^\circ$ ) and minor ( $135^\circ$ ) axis of the molecular emission. The color scale starts at a signal-to-noise ratio of 5. In the first- and second-moment maps, the contour spacing is shown as  $\Delta v$ , in  $\text{km s}^{-1}$ . Notice the velocity shift in the PV diagrams of CO 2–1 and HI. For discussion, see Sects. 3.2, and 4.1.1.

**Table 2.** Properties of continuum emission in NGC 4418.

Freq. GHz	Flux dens. (peak, int.) $\text{mJy beam}^{-1}$ , mJy	Beam maj $\times$ min, PA	Source Size $circ. aver.$	K/Jy
MERLIN:				
1.4	14 (0.3), 38 (2)	$0''.35 \times 0''.16$ , $23^\circ$	$0''.5$ , 80 pc	$1.1 \times 10^7$
5	8 (0.2), 34 (2)	$0''.13 \times 0''.04$ , $19^\circ$	$0''.15$ , 25 pc	$1.0 \times 10^7$
SMA:				
230	57 (1), 59 (1)	$0''.48 \times 0''.38$ , $62^\circ$	$<0''.4$ , 65 pc	121
242	56 (1), 57 (1)	$0''.48 \times 0''.38$ , $62^\circ$	$<0''.4$ , 65 pc	123
273	61 (2), 61 (1)	$0''.41 \times 0''.33$ , $64^\circ$	$<0''.3$ , 50 pc	122
285	65 (4), 65 (1)	$0''.41 \times 0''.33$ , $64^\circ$	$<0''.3$ , 50 pc	122

**Notes.** For the flux density we report the peak value in mJy/beam, and the total integrated flux density in mJy (rms values are shown in parentheses). The circle-averaged source sizes were computed via visibility-fits in the  $u-v$  (see Fig. A.1), for unresolved emission we report upper limits.

at rest (LSR) velocities lower than  $2000 \text{ km s}^{-1}$ . The asymmetric line is well fit by two Gaussian velocity components, with centers at  $2150$  and  $2090 \text{ km s}^{-1}$ , and FWHM line widths of  $134$  and  $160 \text{ km s}^{-1}$ , respectively. The results of the fit are shown in Table 3.

### 3.3. 1 mm continuum

The 1-mm continuum was extracted from the line-free channels in each side-band of the SMA observations. Maps of the continuum emission in the four bands are shown in Fig. 1.

A circle-averaged source size was calculated from visibility fits (see Fig. A.1); the results are reported in Table 2. The emission is unresolved in all 1-mm bands, with upper limits for the angular size of the emission of  $0''.4$  for the LSB and USB of the 230 GHz tuning and  $0''.3$  for the two sidebands of the 270 GHz tuning, corresponding to linear extents of 60 and 45 pc.

Total flux densities range from 59 mJy at 230 GHz to 65 mJy at 285 GHz. Given these results, we assume a 1-mm flux density of 60 mJy confined in a region smaller than 50 pc in diameter. The Jansky-to-Kelvin conversion factor for our SMA observations is roughly 122, which gives a lower limit for the brightness temperature of the 1-mm continuum of 70 K. The presence of a compact 1-mm core is consistent with earlier SMA observations (Sakamoto et al. 2013), where we find part of the continuum at 860 and  $450 \mu\text{m}$  to be emerging from a region of less than  $0''.1$  in diameter, with a brightness temperature higher than 100 K.

### 3.4. Molecular emission

In Fig. 5 we show the spectra in the SMA bands, extracted from the central beam and continuum-subtracted. We identified the molecular emission lines by comparing the observed spectrum with the molecular line database Splatalogue<sup>4</sup>, which includes transitions from the CDMS (Müller et al. 2005), JPL (Pickett et al. 1998) and Lovas/NIST<sup>5</sup> spectral line catalogs as well as the Spectral Line Atlas of Interstellar Molecules (SLAIM)<sup>6</sup>. The narrow line widths found in NGC 4418 ( $\Delta v \simeq 100 \text{ km s}^{-1}$ ) limit line blending, facilitating the identification of molecular transitions. Where line blending is present, we derived line parameters via multi-component Gaussian fitting and by comparing our observations with a local thermal equilibrium (LTE) synthetic spectrum (see Sect. 4.2.1 for discussion).

We detect emission lines of several molecular species, including CO,  $\text{C}^{34}\text{S}$ , HNC and  $\text{HC}_3\text{N}$ , with typical rms of  $5 \text{ mJy beam}^{-1}$  at 230 GHz, and  $10 \text{ mJy beam}^{-1}$  at 270 GHz. The integrated intensity maps of the detected molecular transitions are shown in Fig. 2, while in Table 3 we report the results from Gaussian fitting of the line profiles.

<sup>4</sup> <http://www.splatalogue.net/>

<sup>5</sup> <http://www.nist.gov/pml/data/micro/index.cfm>

<sup>6</sup> Available at <http://www.splatalogue.net/>

**Table 3.** Properties of spectral lines detected in NGC 4418.

Line	Rest frequency [GHz]	$E_u$ [K]	Peak flux [mJy]	$T_b$ [K]	$v_c$ [km s <sup>-1</sup> ]	$\Delta v$ [km s <sup>-1</sup> ]	Source size <i>circ. aver.</i>	
HI	1.420	0.07	$-6 \pm 0.5$	–	$2153 \pm 11$	$131 \pm 12$	$>0.5''$ , 80 pc	
	"	"	$-2 \pm 0.5$	–	$2094 \pm 22$	$160 \pm 18$	$>0.5''$ , 80 pc	
CO 2–1	230.538	17	$439 \pm 6$	$80 \pm 0.6$	$2091 \pm 3$	$163 \pm 6$	$0.7''$ , 120 pc	
	"	"	$140 \pm 6$	$26 \pm 0.6$	$2182 \pm 13$	$165 \pm 11$	$0.7''$ , 120 pc	
HC <sub>3</sub> N 25–24, $v_6 = 1e$	227.793	860	$9 \pm 6$	$>2.2 \pm 1.4$	2120*	100*	$<0.4''$ , 65 pc	
HC <sub>3</sub> N 25–24, $v_6 = 1f$	227.970	860	$9 \pm 6$	$>2.2 \pm 1.4$	$2122 \pm 9$	$93.8 \pm 19$	$<0.4''$ , 65 pc	
HC <sub>3</sub> N 25–24, $v_7 = 1e$	227.977	463	$36 \pm 6$	$>8.8 \pm 1.4$	2120*	100*	$<0.4''$ , 65 pc	
HC <sub>3</sub> N 25–24, $v_7 = 1f$	228.303	463	$36 \pm 6$	$>8.8 \pm 1.4$	2120*	100*	$<0.4''$ , 65 pc	
HC <sub>3</sub> N 25–24, $v_7 = 2$	228.858	787	$12 \pm 6$	$>3.0 \pm 1.4$	2120*	100*	$<0.4''$ , 65 pc	
C <sup>34</sup> S 5–4	241.016	28	$43 \pm 3$	$13 \pm 1$	$2143 \pm 4$	$77 \pm 11$	$0.35''$ , 57 pc	
HNC (a)	HNC 3–2	271.981	26	$167 \pm 7$	$>40.6 \pm 1.6$	2090*	$130 \pm 17$	$<0.3''$ , 50 pc
	"	"	"	$54 \pm 7$	$>13.2 \pm 1.6$	2180*	$141 \pm 21$	$<0.3''$ , 50 pc
HNC (b)	HNC 3–2	271.981	26	$167 \pm 7$	$>40.6 \pm 1.6$	2100*	$130 \pm 17$	$<0.3''$ , 50 pc
	HNC, $v_2 = 1e$	271.924	692	$43 \pm 7$	$>10.4 \pm 1.6$	2100*	$85 \pm 21$	$<0.3''$ , 50 pc
HC <sub>3</sub> N 30–29	272.884	203	$79 \pm 7$	$>19.2 \pm 1.6$	$2140 \pm 11$	$115 \pm 6$	$<0.3''$ , 50 pc	
HC <sub>3</sub> N 30–29, $v_6 = 1e$	273.331	921	$13 \pm 7$	$>3.2 \pm 1.6$	2120*	80*	$<0.3''$ , 50 pc	
HC <sub>3</sub> N 30–29, $v_6 = 1f$	273.546	921	$13 \pm 7$	$>3.2 \pm 1.6$	2120*	80*	$<0.3''$ , 50 pc	
HC <sub>3</sub> N 30–29, $v_7 = 1e$	273.553	524	$40 \pm 7$	$>9.8 \pm 1.6$	2120*	80*	$<0.3''$ , 50 pc	
HC <sub>3</sub> N 30–29, $v_7 = 1f$	273.944	524	$40 \pm 7$	$>9.8 \pm 1.6$	2120*	$78 \pm 12$	$<0.3''$ , 50 pc	
HNC 3–2, $v_2 = 1f$	273.869	692	$55 \pm 7$	$>13.4 \pm 1.6$	2100*	$78 \pm 11$	$<0.3''$ , 50 pc	
HC <sub>3</sub> N 31–30, $v_6 = 1f$	282.660	934	$13 \pm 10$	$>3.2 \pm 2.4$	2100*	80*	$<0.3''$ , 50 pc	
HC <sub>3</sub> N 31–30, $v_7 = 1e$	282.668	538	$39 \pm 10$	$>9.4 \pm 2.4$	2100*	80*	$<0.3''$ , 50 pc	
HC <sub>3</sub> N 31–30, $v_7 = 1f$	283.072	538	$39 \pm 10$	$>9.4 \pm 2.4$	$2112 \pm 11$	$82 \pm 25$	$<0.3''$ , 50 pc	

**Notes.** Results of Gaussian fitting are shown together with circle-averaged source sizes. Line-peak flux densities refer to the flux density integrated on the central clean beam. We converted the flux density to main-beam brightness  $T_{mb}$  by applying the K/Jy conversion factor of Table 2. For the resolved emission, we report the deconvolved brightness temperature  $T_b$ , or its lower limit in the case of unresolved emission. Errors on the measured flux densities and brightness temperatures are reported in parentheses. Line-center velocities  $V_c$  are LSR optical velocities. For HNC 3–2, for which two alternative fits are possible, these are labeled with (a) and (b), see Sect. 3.4.2. Source sizes are FWHM sizes derived from fitting circle-averaged visibilities with circular Gaussian profiles (see Fig. A.1). For strong line blending, the velocity and line width of the emission were fixed to the values derived for blend-free transitions. Fixed values are marked with an asterisk in the table.

### 3.4.1. CO $J = 2-1$

Bright CO  $J = 2-1$  emission was detected in NGC 4418. The emission is spatially resolved (see Fig. A.1), and the integrated intensity can be fit well by an elliptical Gaussian with major axis  $0''.75$  and minor axis  $0''.45$ , corresponding to 120 and 70 pc at the galaxy distance, and a position angle of  $45^\circ$ . The spectral line profile is skewed toward high velocities and is fit well by two Gaussian components, with LSR velocities of 2090 and 2180 km s<sup>-1</sup> (see Sect. 4.1.1 for a more detailed discussion) and full-width-at-half-maximum (FWHM) line widths of 160 km s<sup>-1</sup>. We estimate a deconvolved brightness temperature of 80 and 26 K for the low-velocity and high-velocity component, respectively.

The first-moment map of CO 2–1 (see Fig. 3) shows a shallow but well-defined velocity gradient perpendicular to the major axis of the galaxy. This velocity shift is also revealed by the position-velocity diagram at  $135^\circ$  in Fig. 3, as a slight asymmetry of roughly 500 m s<sup>-1</sup> pc<sup>-1</sup> in the SE-NW direction. In the PV diagram along the major axis ( $45^\circ$ ), we find no clear sign of rotation. The only noticeable feature is a broadening of the CO line toward the center of the Galaxy, which is also evident from the

second-moment map in Fig. 3. A more detailed discussion on the CO 2–1 dynamics is given in Sect. 4.1.1.

### 3.4.2. HNC $J = 3-2$

The HNC  $J = 3-2$  emission line was detected in the 270 GHz SMA band. Both 2D-Gaussian fitting in the image domain, and visibility fitting in the  $u-v$ , show that the HNC-emitting region is marginally resolved, with an angular diameter between  $0''.2$  and  $0''.3$ , corresponding to 30–50 pc at the galaxy distance (see Appendix A.1).

The line profile appears skewed, with an evident excess at high velocities (see Figs. 4 and 5f). Two possible scenarios, described in Table 3, fit the observed HNC emission: a) two velocity components at 2090 km s<sup>-1</sup> and 2180 km s<sup>-1</sup>, corresponding to those found for the CO 2–1 emission; b) a blend with the  $J = 3-2$  transition of the  $v_2 = 1e$  vibrationally excited state of HNC.

This last scenario is supported by the detection of the  $J = 3-2$ ,  $v_2 = 1f$  transition of HNC at 273.869 GHz (see Fig. 5). The line is partially blended with  $J = 30-29$  emission of vibrationally excited HC<sub>3</sub>N, but the two lines are separated far enough in velocity to be clearly separated. The strength of the

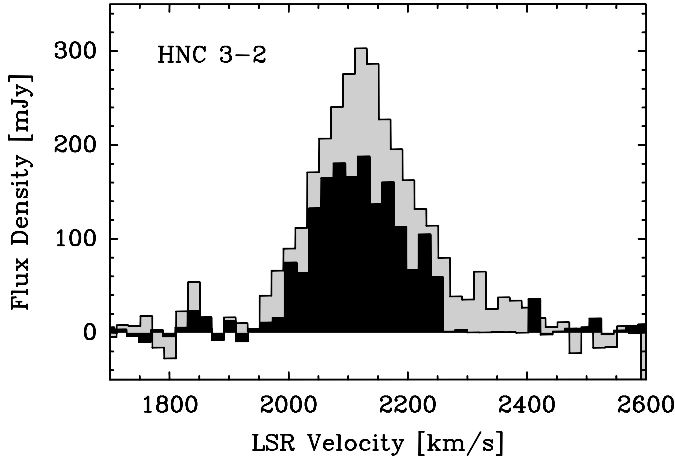


**Fig. 4.** Comparison of HNC 3–2 emission observed by the IRAM 30 m telescope (gray) and with SMA (black).

$v_2 = 1f$  line is consistent with the HNC  $J = 3-2$ ,  $v = 0$  line being blended with  $v_2 = 1e$  emission. To our knowledge, this is the first extragalactic detection of mm-wave emission from vibrationally excited HNC. In Fig. 5 we only show the fit for this second scenario, but we cannot exclude that the HNC 3–2 line receives a significant contribution from the high-velocity component at  $2180 \text{ km s}^{-1}$ . Most probably, both vibrational excitation and a second velocity component work together in shaping the observed profile.

The peak flux density of the HNC  $J = 3-2$  transition detected by the SMA is roughly 70% of the flux density obtained by single-dish observations with the IRAM 30-m telescope (Fig. 4). Our observations were made with the extended configuration of the SMA, with a minimum projected baseline of 80 m, which converts into a maximum detectable source size of  $3''$ . The missing flux thus may be coming from an extended component ( $>1''.5$ ) that is resolved out by our SMA observations. This interpretation is also suggested by the line profile, which is wider for the SMA spectrum, as we would expect if an extended, narrow component had been filtered out because of the incomplete uv-coverage.

### 3.4.3. $\text{HC}_3\text{N}$

The  $\text{HC}_3\text{N}$  molecule is detected in the vibrational ground state and in the  $v_7 = 1$  and  $v_6 = 1$  excited levels (see Fig. 5). The emission is unresolved at all observed wavelengths (see Fig. A.1), which gives an upper limit for the diameter of the  $\text{HC}_3\text{N}$ -emitting region of about 50 pc ( $0''.3$ ).

The brightest  $\text{HC}_3\text{N}$  emission ( $\sim 80 \text{ mJy}$ ,  $T_b \simeq 20 \text{ K}$ ) comes from the  $J = 30-29$  transition of the ground vibrational state ( $v = 0$ ) at  $272.884 \text{ GHz}$ . A Gaussian fit of the line profile reveals an emission velocity of  $2110 \text{ km s}^{-1}$  and a FWHM dispersion of  $125 \text{ km s}^{-1}$  (see Table 3).

The  $v_7 = 1$  vibrationally excited state of  $\text{HC}_3\text{N}$  is detected in the  $J = 25-24$ ,  $J = 30-29$  and  $J = 31-30$  rotational transitions, with a peak flux density of roughly half the  $J = 30-29$ ,  $v = 0$  flux density in all bands. The  $v_7 = 1$  and  $v_6 = 1$  states are doublets, with single states labeled  $e$  and  $f$ , depending on the parity of the wave function (Yamada & Creswell 1986). The  $v_7 = 1e$  and  $v_6 = 1f$  lines are only  $\sim 10 \text{ MHz}$  apart and are often blended. For this reason, the line properties of  $v_7 = 1$  and  $v_6 = 1$  emission were derived by Gaussian fitting of the blend-free lines, i.e., the  $v_7 = 1f$  and  $v_6 = 1e$  transitions.

Gaussian fitting shows that  $v_7 = 1$  and  $v_6 = 1$  transitions have similar velocity centroids ( $v_c \simeq 2100 \text{ km s}^{-1}$ ) and line dispersions ( $\Delta v \simeq 100 \text{ km s}^{-1}$ ), with the peak intensity of the  $v_6 = 1$  emission being roughly half the  $v_7 = 1$ .

A tentative detection,  $3\sigma$  in integrated flux density, of the  $J = 25-24$ ,  $v_7 = 2$  triplet of  $\text{HC}_3\text{N}$  at  $228 \text{ GHz}$  is also reported in Table 3 and Fig. 5e. For a discussion of the vibrational excitation of  $\text{HC}_3\text{N}$  in NGC 4418 see Sect. 4.2.2.

### 3.4.4. $\text{C}^3\text{S}$

The  $J = 5-4$  rotational transition of  $\text{C}^3\text{S}$  at  $241 \text{ GHz}$  is clearly detected in our SMA spectrum (see Fig. 5). The emission is marginally resolved, as results from 2D Gaussian fitting and  $u-v$  visibility fits (see Fig. A.1), with a source size of  $0''.35$ , corresponding to  $\sim 57 \text{ pc}$  in the source plane. A Gaussian fit of the line profile reveals an emission velocity of  $2120 \text{ km s}^{-1}$  and a line width of  $77 \text{ km s}^{-1}$  (see Table 3).

## 4. Discussion

### 4.1. Gas dynamics and kinematics

#### 4.1.1. CO 2–1 modeling

By comparing the PV diagrams of HI and CO, it is clear that the two lines have different velocities, with the peak of HI absorption redshifted by roughly  $60 \text{ km s}^{-1}$  from the peak of CO emission. This shift is confirmed by comparing the spectra extracted from the central clean beam for the two transitions, which are shown in Figs. 5c, d. The CO profile is asymmetric and is best fit by two Gaussian components: a  $440 \text{ mJy}$  component at  $2090 \text{ km s}^{-1}$  and a redshifted  $140 \text{ mJy}$  component at  $2180 \text{ km s}^{-1}$ , both with FWHM line widths of  $160 \text{ km s}^{-1}$  (see Table 3 for details). HI absorption and CO emission show specular line profiles: both show a systemic component (SC) at  $2090 \text{ km s}^{-1}$  and a redshifted component (RC), but while the SC is the brightest of the two for CO, the HI absorption is dominated by the RC.

Without a clear detection of rotation in the CO data cube, the systemic velocity of the galaxy is poorly constrained and the choice of the  $2090 \text{ km s}^{-1}$  component as systemic was made only because of its brightness in the CO spectrum. However, the velocity of the SC component is consistent with the peak velocities of single-dish spectra (e.g., Aalto et al. 2007a; Costagliola & Aalto 2010) and with observations of HCN 4–3 reported in Sakamoto et al. (2013), which show a velocity gradient along the major axis of the galaxy. If HCN is tracing the rotation of the inner disk, these observations set the systemic velocity of NGC 4418 at  $2088 \text{ km s}^{-1}$ , which coincides with our SC component.

To study the kinematics traced by the CO 2–1 emission, we built a simple model, composed of two elliptical 3D Gaussian components (with coordinates RA, Dec, and  $V_{\text{LSR}}$ ) with the aim of reproducing the velocity gradient observed in the first-moment map and PV diagram, and the integrated intensity profile. Each component is characterized by its position on the sky (center of the ellipse), its dimensions (major axis, minor axis, position angle), the peak intensity, and by its kinematics (LSR velocity and line width). The size and position of the two components were found by fitting the channel-averaged visibilities with the UV\_FIT routine of the MAPPING software. A least-squares minimization in the image domain was then used to derive LSR velocities and line widths. We assumed the two

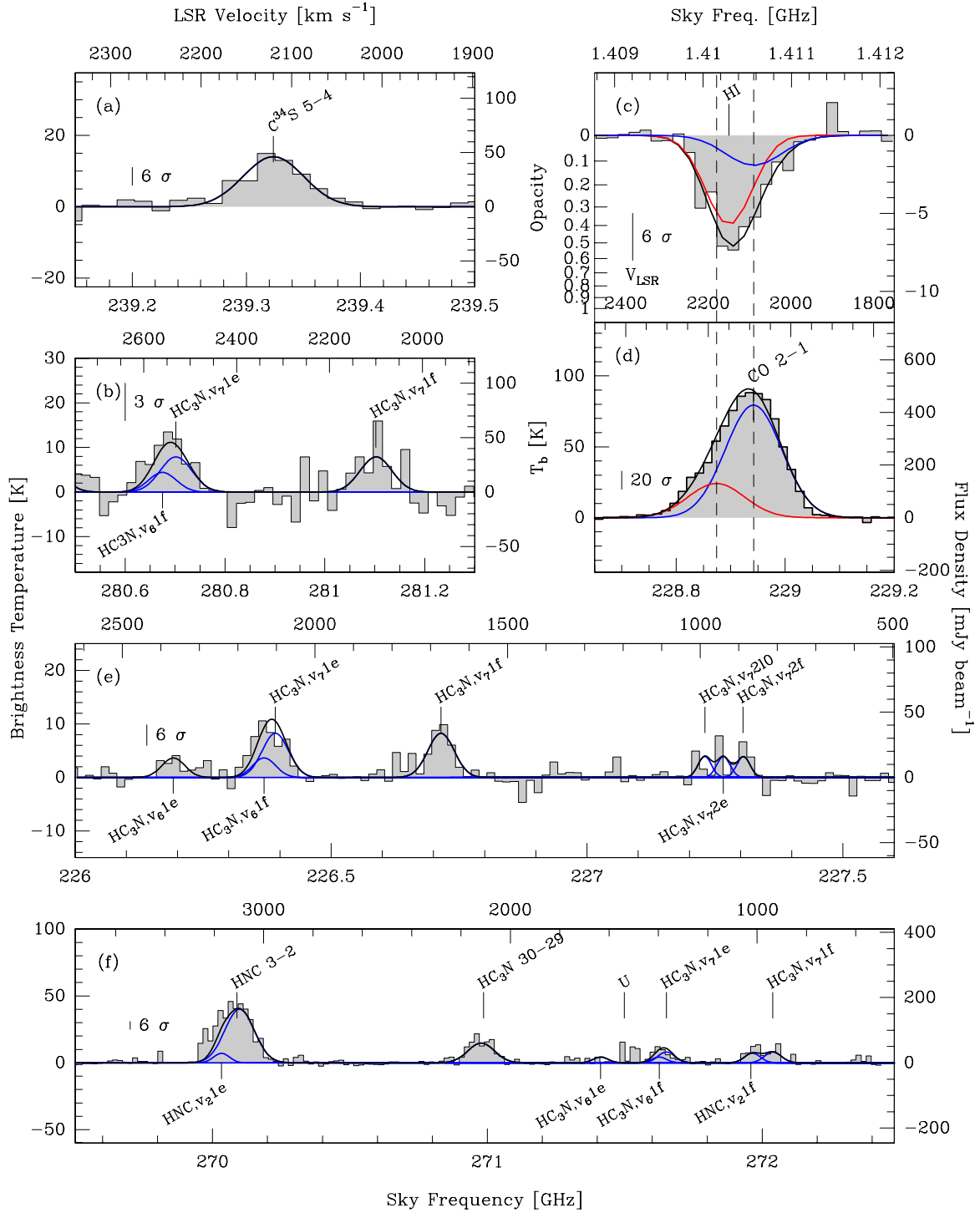


**Fig. 5.** Spectra extracted from the central beam of MERLIN and SMA observations in NGC 4418. The data are drawn as shaded histogram, the solid black line represents the total profile of our LTE best-fit model, and LTE emission from single molecular species is drawn in blue. Panels **c)** and **d)** show a comparison of HI and CO 2–1 profiles. Dashed vertical lines mark the velocity centroid of the two components of CO emission, SC at 2090 and RC at 2180 km s<sup>−1</sup> LSR (see Sect. 4.1.1). The redshifted Gaussian components (RC), associated with a possible in-flow, are drawn in red in both panels. The conversion between flux density and brightness temperature is discussed in Sect. 4.2.1. The results of the Gaussian fit for each line are shown in Table 3.

components to be separated far enough in velocity to be considered independent as far as radiative transfer is concerned. We therefore did not include radiative transfer in our model. This is discussed in more detail in Sect. 4.2.1.

The parameters that fit the data cube are reported in Table 4. The model is consistent with two main velocity components, a systemic component at 2090 km s<sup>−1</sup> (SC) and redshifted

emission at 2180 km s<sup>−1</sup> (RC). The two components have similar sizes and orientation, but appear to be slightly displaced, with an offset of about 0'.1 in the SE–NW direction. This offset between the two components is responsible for the observed velocity gradient at PA 135°. This simple model can reproduce 90% of the observed CO emission, a comparison with the data is shown in Fig. 6.

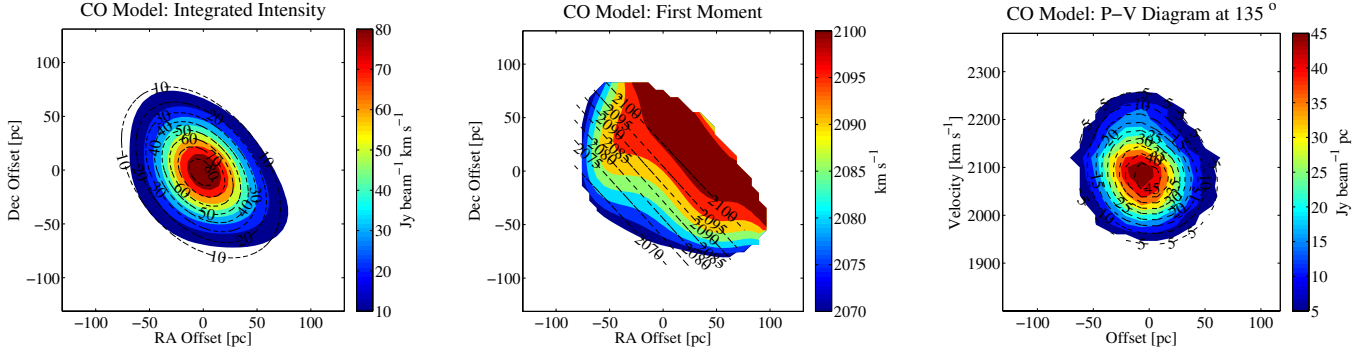


**Fig. 6.** Model of the CO 2–1 emission overlaid as dashed contours over the color map of the observed data. The parameters of the model are reported in Table 4, for discussion see Sect. 4.1.1.

#### 4.1.2. Atomic and molecular in-flow

In Sects. 3.2 and 4.1.1 we showed that HI absorption and CO 2–1 emission can be fit by two velocity components at 2090 (SC) and 2150–2180 (RC)  $\text{km s}^{-1}$ . If we assume the SC component to be the systemic velocity of the galaxy (see discussion in Sect. 4.1.1), the RC component observed in HI absorption is tracing redshifted foreground gas moving toward the center of the galaxy, and it may therefore be interpreted as an in-flow signature. In this scenario, the SC component in the CO 2–1 spectrum could be tracing a molecular component of the same in-flowing gas. This interpretation assumes the RC components of HI and CO 2–1 to be roughly co-spatial, which is a reasonable assumption given the similar velocities in the two tracers. However, the sensitivity of our HI data is not good enough to reliably constrain the morphology of the redshifted absorption, therefore we cannot rule out other possible interpretations.

A spherical molecular in-flow in the core of NGC 4418 was first suggested by González-Alfonso et al. (2012) to explain the redshifted OH absorption observed by the *Herschel* satellite. The presence of an atomic and molecular in-flow in NGC 4418 would not be surprising. The galaxy and its interacting companion are in fact linked by an atomic hydrogen bridge (Klöckner et al., in prep.), and it is very likely that part of that intergalactic material is being funneled into the potential well of the most massive galaxy of the pair.

The HI absorption may be tracing part of this atomic gas falling on the galaxy’s nucleus along our line of sight. From our observations it is not possible to detail the morphology of the in-flow, thus we cannot confirm whether the material is channeled toward the nucleus by a spiral arm or by a spherically symmetric flow. However, because of the 0’1 shift between SC and RC components and the lack of significant blueshifted emission, our CO 2–1 model does suggest the possible in-flow not to be spherically symmetric. Indeed, near-IR images of NGC 4418 by Evans et al. (2003) show dark radial features, that could be interpreted as dust lanes connecting the nucleus with the outer regions of the galaxy (see Figs. 1 and 2 in Evans et al. 2003). These structures may contain enough molecular and atomic gas to produce the observed redshifted component.

#### 4.1.3. Atomic and molecular mass

The column density of the in-flowing atomic gas can be calculated from the observed HI opacity, following Rohlfs & Wilson (1996):

$$\frac{N(\text{H})}{\text{cm}^{-2}} \simeq 1.82 \times 10^{18} \times \frac{T_s}{\text{K}} \times \int \tau(v) \times \frac{dv}{\text{km s}^{-1}}, \quad (1)$$

**Table 4.** Parameters for the two-components model for CO 2–1 emission.

	Component 1 (SC)	Component 2 (RC)
(RA, Dec) <sup>1</sup>	0.03”, –0.03”	–0.05”, 0.05”
(maj, min, PA) <sup>2</sup>	0.75”, 0.49”, 45°	0.75”, 0.4”, 45°
Peak <sup>3</sup>	440 mJy	140 mJy
( $V_c$ , $\Delta V$ ) <sup>4</sup>	2090, 160 $\text{km s}^{-1}$	2180, 160 $\text{km s}^{-1}$
$M(\text{H}_2)$ <sup>5</sup>	0.6–2.5 $\times 10^8 M_\odot$	1–4.2 $\times 10^7 M_\odot$
$M(\text{H})$ <sup>6</sup>	4.9 $\pm$ 2.9 $\times 10^5 M_\odot$	1.2 $\pm$ 0.2 $\times 10^6 M_\odot$
$M(\text{H}_2) + M(\text{H})$ <sup>7</sup>	0.6–2.5 $\times 10^8 M_\odot$	1.1–4.3 $\times 10^7 M_\odot$

**Notes.** The model is described in Sect. 4.1.1, while the mass estimates are discussed in Sect. 4.1.2. <sup>(1)</sup> Offsets of the Gaussian component from the phase center. <sup>(2)</sup> Major axis, minor axis and, the position angle of the 2D Gaussian. <sup>(3)</sup> Peak intensity of the CO line. <sup>(4)</sup> Velocity and FWHM of the CO line. <sup>(5)</sup> Molecular mass calculated from the CO intensity (Sect. 4.1.3). <sup>(6)</sup> Atomic mass calculated from the HI opacity (Sect. 4.1.3). <sup>(7)</sup> Total hydrogen mass. The CO 2–1 model and the derived gas masses are discussed in Sects. 4.1.1 and 4.1.3.

where  $T_s$  is the spin temperature of HI. If we assume a Gaussian line profile and an elliptical Gaussian absorbing region with major axis maj and minor axis min, the mass of HI is then

$$\frac{M(\text{H})}{M_\odot} \simeq 2.3 \times 10^{-2} \times \frac{T_s}{\text{K}} \times \tau_p \times \frac{\Delta v}{\text{km s}^{-1}} \frac{\text{maj} \times \text{min}}{\text{pc}^2}, \quad (2)$$

where  $\tau_p$  is the peak opacity and  $\Delta v$  is the velocity dispersion of the HI profile.

The peak opacities of the two velocity components of HI are  $0.5 \pm 0.08$  (RC) and  $0.2 \pm 0.1$  (SC). If we assume the atomic hydrogen gas to have the same kinetic temperature as the CO 2–1 peak emission, i.e.,  $T_s \simeq T_{\text{CO}} = 80$  K, we find the HI column density toward the core of NGC 4418 to be  $1.5 \pm 0.2 \times 10^{22}$  and  $5.8 \pm 2.9 \times 10^{21} \text{ cm}^{-2}$  for the RC and SC components, respectively. This calculation assumes the atomic and molecular gas to be co-spatial and to have the same excitation temperature, which in general may not be true. For a multi-phase clumpy medium, we would expect HI to have a higher temperature than CO, thus the values derived for the hydrogen column density should be considered as lower limits.

The size of the HI absorption is determined by the structure of the background continuum emission and it is only a lower limit to the extent of the atomic gas. To calculate the total HI mass and compare it with the total molecular mass, we assumed the atomic gas to have the same spatial extent as the

CO 2–1 emission. In this case, Eq. (2) gives an atomic hydrogen mass of  $1.2 \pm 0.2 \times 10^6$  and  $4.9 \pm 2.9 \times 10^5 M_{\odot}$  for the RC and SC component.

In principle, the molecular hydrogen mass contained in the system can be calculated by applying an appropriate CO-H<sub>2</sub> conversion factor ( $X_{\text{CO}}$ ). Surveys of CO 1–0 emission in LIRGs (e.g., Solomon et al. 1997; Yao et al. 2003) found values of  $X_{\text{CO}}$  three to ten times lower than what was found for Galactic giant molecular clouds (GMCs). This is usually attributed to the high turbulence in the cores of LIRGs. However, a recent study by Papadopoulos et al. (2012) suggested that in the warm and dense nuclei of LIRGs and ULIRGs, low- $J$  CO lines may not be good tracers of the total molecular mass. For objects with available observations of high-density tracers (e.g., high- $J$  CO, HCN), these authors found  $X_{\text{CO}}$  to be similar to the Galactic value and suggested that this could be a common property of LIRGs and ULIRGs nuclei. In the following analysis we consider a conversion factor ranging from the classical ULIRG value of  $1 M_{\odot} (\text{km s}^{-1} \text{pc}^{-2})^{-1}$  to a Galactic value of  $4 M_{\odot} (\text{km s}^{-1} \text{pc}^{-2})^{-1}$  (Papadopoulos et al. 2012).

Single-dish observations by Aalto et al. (2007a) revealed a CO 2–1/1–0 brightness temperature ratio of roughly 0.5 when corrected for a source size of  $0''.7$ . For a conversion factor  $X_{\text{CO}} = 1\text{--}4 M_{\odot} (\text{km s}^{-1} \text{pc}^{-2})^{-1}$  we find a molecular hydrogen mass of  $0.6\text{--}2.5 \times 10^8 M_{\odot}$  for the SC component and  $1\text{--}4.2 \times 10^7 M_{\odot}$  for RC by integrating on the CO 2–1 data-cube. In the inner 100 pc, this corresponds to averaged H<sub>2</sub> column densities of  $1.2\text{--}4.9 \times 10^{23} \text{cm}^{-2}$  for the redshifted emission and  $0.7\text{--}2.9 \times 10^{24} \text{cm}^{-2}$  for the systemic component. Given the uncertainties, these values agree well with the molecular mass of  $\sim 10^8 M_{\odot}$  estimated by Sakamoto et al. (2013) from 850  $\mu\text{m}$  continuum observations and HCN 4–3 kinematics in the inner 20 pc of the galaxy.

The molecular-to-atomic-mass ratio  $M(\text{H}_2)/M(\text{H})$  is 40–370 for SC and 12–300 for RC. Despite the large scatter due to the uncertainties on  $X_{\text{CO}}$ , we see that  $M(\text{H}_2)$  is at least one order of magnitude greater than  $M(\text{H})$  in both components, with a hint of a higher molecular fraction in the SC. A similar result, less dependent on the assumptions used to derive molecular and atomic gas masses, can be derived from the spectra in Fig. 5. In general, the mass contained in the beam can be expressed as  $M(\text{H}) = G(\text{H}) \times \Delta v \times \alpha$  and  $M(\text{H}_2) = G(\text{CO}) \times \Delta v \times \beta$ , where  $G$  and  $\Delta v$  are the Gaussian amplitudes and line widths listed in Table 3, and  $\alpha$  and  $\beta$  are conversion factors (see e.g., Eq. (2)). If we assume the excitation conditions to be the same for the two velocity components,  $\alpha$  and  $\beta$  are the same for SC and RC, and we obtain

$$R_{\text{Mol}} \equiv \frac{M(\text{H}_2)_{\text{SC}}/M(\text{H})_{\text{SC}}}{M(\text{H}_2)_{\text{RC}}/M(\text{H})_{\text{RC}}} = \frac{G(\text{CO})_{\text{SC}}\Delta v}{G(\text{H})_{\text{SC}}\Delta v} \times \frac{G(\text{H})_{\text{RC}}\Delta v}{G(\text{CO})_{\text{RC}}\Delta v}, \quad (3)$$

which is independent of conversion factors. By substituting values from Table 3, we find  $R_{\text{Mol}} = 8 \pm 2$ , which confirms an higher molecular-to-atomic-mass ratio in the SC component. If we assume the SC component to be dominated by the gas in the nucleus and the RC to be mostly coming from the in-flowing envelope, these molecular ratios may suggest a density and pressure gradient that increases toward the inner regions of the galaxy. However, because of the many uncertainties involved, and because we do not have the resolution to resolve the geometry of the in-flow, this is at present just an educated speculation based on the limited observations.

If we assume the HI absorption and CO 2–1 emission to be distributed on a similar scale of  $\sim 80$  pc, the total gas mass contained in the in-flow is  $M_{\text{In}} = M(\text{H}_2) + M(\text{H}) = 1\text{--}4.3 \times 10^7 M_{\odot}$ . Assuming a spherical geometry, the estimated in-flow mass

would result in a gas density of  $\sim 10^3 \text{cm}^{-3}$ , which is reasonable for CO 2–1 emitting gas (the critical density of CO 2–1 is  $n_{\text{crit}} \sim 10^3 \text{cm}^{-3}$ ).

The mass flux depends on the geometry of the in-flowing gas. If we assume a projected size of the in-flow along the line of sight of  $\Delta \ell \approx 80$  pc (i.e., a spherical geometry), the total gas mass flux toward the nuclear regions of NGG 4418 can be calculated as  $\dot{M} \approx M_{\text{In}} \times \Delta v \times \Delta \ell$ , where  $\Delta v \approx 90 \text{km s}^{-1}$  is the velocity shift between the SC and RC components. We find  $\dot{M} \approx 11\text{--}49 M_{\odot} \text{yr}^{-1}$ . This value strongly depends on the assumed projected size of the in-flowing gas and must be considered as an order-of-magnitude estimate. A comparison with the in-flow model derived by González-Alfonso et al. (2012) is presented in Sect. 4.3.

#### 4.1.4. Outflow/in-flow scenario

In a companion paper (Sakamoto et al. 2013), a U-shaped red feature was found in an optical color-index map, obtained as the ratio of  $(i' + z')/(g' + r')$  SDSS images. This is suggested to be associated to a minor-axis outflow, extending to  $10''$  (1.5 kpc on the sky) on the northwestern side of the galaxy. The complex CO 2–1 and 3–2 velocity fields would then be the result of a mixed in-flow/outflow system. We speculate that the observed redshifted CO and HI could be tracing an in-flow on the plane of the galaxy, along the line of sight, while the U-shaped absorption feature would be tracing an outflow perpendicular to the plane. For a more detailed discussion about the possible outflow, refer to Sect. 3.6 in Sakamoto et al. (2013).

In the same paper (Sect. 3.4), an alternative explanation for the skewed CO 3–2 profile as the result of redshifted self-absorption was discussed as well. With the data at hand it is difficult to separate the two suggested models for CO emission, and we suggest the two interpretations as two equally probable scenarios. Both interpretations are consistent with the molecular in-flow detected by González-Alfonso et al. (2012) with *Herschel* observations (see discussion in Sect. 4.3).

## 4.2. Molecular excitation

### 4.2.1. Local thermal equilibrium analysis of the identified molecular lines

The high velocity dispersions found for extragalactic molecular emission ( $\sim 1000 \text{km s}^{-1}$ ) often make the identification of spectral lines a challenging task. In the most extreme cases, when blending and line confusion make it almost impossible to achieve an unambiguous Gaussian fit to the single spectral features, an effective technique is fitting a synthetic spectrum to the data (e.g., Martín et al. 2011). Even in our case, despite the narrow (for an extragalactic object) line widths found in NGC 4418 ( $\sim 100 \text{km s}^{-1}$ ), significant line blending is present, especially for the faint transitions of vibrationally excited molecules. The observed spectra were therefore fitted with a LTE synthetic emission model.

Our model calculates the integrated brightness spectrum of a molecule, starting from an estimate of the molecule's column density  $N$  and excitation temperature  $T_{\text{ex}}$ , and assuming local thermal equilibrium. The transition parameters necessary for calculating LTE intensities were taken from the molecular line database Splatalogue.

For molecules with many different transitions detected in the observed bands, a rotational-diagram analysis (e.g., Goldsmith & Langer 1999) of the blend-free lines was first attempted, to

assign an appropriate starting value for  $T_{\text{ex}}$ . For molecules with only one transition observed in the SMA bands, it was not possible to solve the degeneracy between column density and excitation temperature, and a fixed value was chosen for  $T_{\text{ex}}$ . The integrated intensities calculated by the LTE code were then converted into brightness temperature spectral profiles by convolution with a Gaussian. The FWHM of the convolving line profile was set by Gaussian fitting the blend-free lines or was fixed at  $100 \text{ km s}^{-1}$  when this was not possible.

To compare the LTE model with our observations, we converted the flux density spectrum into Jy, extracted from the central synthesized beam, to main-beam temperature units using

$$T_{\text{mb}}/S = \frac{\lambda^2}{2k} \Omega_{\text{mb}}^{-1}, \quad (4)$$

where  $T_{\text{mb}}$  is the main-beam synthesized temperature,  $S$  is the main-beam flux density in Jy, and  $\Omega_{\text{mb}}$  is the synthesized beam solid angle. The resulting K/Jy conversion factors for all four observed SMA bands are shown in Table 2, Col. 5.

The brightness temperature of the emission is related to the main-beam temperature by

$$T_{\text{b}} = T_{\text{mb}} \frac{\Omega_{\text{S}\star\text{mb}}}{\Omega_{\text{S}}}, \quad (5)$$

where  $\Omega_{\text{S}\star\text{mb}}$  is the solid angle of the convolution between the source and the synthesized beam. For spatially resolved emission (CO,  $\text{C}^{34}\text{S}$ ) we derived brightness temperature profiles, that can be directly compared with our synthetic spectrum. For unresolved emission, we calculated lower limits to  $T_{\text{b}}$  by assuming a source size of one synthesized beam. Main-beam temperatures and brightness temperatures, derived from Eqs. (4) and (5) for all detected molecular transitions, are shown in Table 3.

We fitted the LTE model to the data by minimizing the rms of the residuals, after subtracting the synthetic spectra from the observations. The excitation temperature of the species for which we did not have more than one transition in our spectra was fixed at  $T_{\text{CO}} = 80 \text{ K}$ , which is the peak brightness temperature of the CO 2–1 emission. If we assume the CO  $J = 2-1$  transition to be optically thick,  $T_{\text{CO}}$  is a good estimate of its excitation temperature, which at LTE is equal to the kinetic temperature of the molecular gas.

For  $v_6 = 1$  and  $v_7 = 1$  vibrationally excited  $\text{HC}_3\text{N}$ , which show several transitions in our SMA bands, it is possible to estimate the rotational temperature via population diagram analysis, resulting in  $T_{\text{ex}} = 310 \text{ K}$  for  $v_6 = 1$  and  $T_{\text{ex}} = 160 \text{ K}$  for  $v_7 = 1$ .

The best-fit column densities derived from our LTE model are listed in Table 5. The model spectrum is shown in Fig. 5.

#### 4.2.2. Vibrational excitation and IR pumping

Vibrational excitation of molecules occurs via stretching and bending modes in the IR. The rotational spectrum of these vibrationally excited molecules can be observed at mm wavelengths and provides important clues about the physical conditions of the emitting region. Critical densities of vibrational transitions are usually higher than the highest densities found in the molecular ISM ( $>10^8 \text{ cm}^{-3}$ , e.g., Schilke et al. 1992), and their excitation is consequently considered to be dominated by radiation. In the limit of optically thick vibrational transitions, the vibrational temperature derived from mm emission of vibrationally excited molecules is a good estimate of the temperature of the IR field in the emitting region. For this reason, vibrationally excited molecular emission has been used by various authors as an

**Table 5.** Results from our LTE model of molecular emission in the SMA spectra.

Molecule	$T_{\text{rot}}$ [K]	$N$ [ $\text{cm}^{-2}$ ]	$T_{\text{vib}}$ [K]
CO (SC)	80*	$>1 \times 10^{20}$	
CO (RC)	80*	$5 \pm 1 \times 10^{18}$	
$\text{C}^{34}\text{S}$	80*	$5 \pm 1 \times 10^{15}$	
HNC $v = 0$	80*	$8 \pm 4 \times 10^{15}$	} $350 \pm 40$
HNC $v_2 = 1$	80*	$2 \pm 1 \times 10^{15}$	
$\text{HC}_3\text{N } v = 0$	80*	$7 \pm 2 \times 10^{16}$	} $315 \pm 30$
$\text{HC}_3\text{N } v_6 = 1$	$310 \pm 50$	$3.6 \pm 2 \times 10^{15}$	
$\text{HC}_3\text{N } v_7 = 1$	$160 \pm 30$	$6 \pm 3 \times 10^{15}$	
$\text{HC}_3\text{N } v_7 = 2$	160*	$4 \pm 2 \times 10^{15}$	

**Notes.** For  $\text{HC}_3\text{N } v_6 = 1$  and  $v_7 = 1$ , the excitation temperature was calculated with the population diagram method. The excitation temperature was fixed at 80 K for species with only one observed transition, while for  $\text{HC}_3\text{N } v_7 = 2$  the rotational temperature was fixed at the value derived for  $\text{HC}_3\text{N } v_7 = 1$  (160 K). The fixed parameters in the fit are marked with asterisks. Vibrational temperatures derived for HNC and  $\text{HC}_3\text{N}$  transitions are also shown. Uncertainties on the excitation temperatures are Monte Carlo estimates. See Sect. 4.2.1 for a discussion. Because of the many uncertainties and assumptions involved, we advise extreme caution when interpreting temperatures and column densities derived by LTE models. Please see Sect. 4.2.3 for a discussion.

extinction-free probe of the IR field in highly obscured objects, both in the Galaxy (e.g., Wyrowski et al. 1999; Schilke et al. 2003) and in extragalactic sources (e.g., Costagliola & Aalto 2010; Sakamoto et al. 2010).

Infrared excitation of vibrational modes may also play an important role in populating the rotational levels of the ground vibrational state (e.g., Carroll & Goldsmith 1981). Recent studies showed that IR-pumping via vibrational modes may affect the intensity of rotational lines of even standard dense gas tracers such as HCN (Sakamoto et al. 2010), HNC (Schilke et al. 2003), and  $\text{HC}_3\text{N}$  (Costagliola & Aalto 2010), especially in regions with high IR fluxes.

Following Carroll & Goldsmith (1981), the  $(J, v = 0)$  state of a molecule can be excited by an IR photon to a  $(J + 1, v = 1)$  vibrationally excited state and then decay either to the starting state or to  $(J + 2, v = 0)$ . In the latter case, we say that the population of the  $J + 2$  level has been pumped by the IR field (see Fig. 8). The pumping rate can be estimated as

$$P \simeq \frac{A_{\text{vib}}}{e^{T_0/T_{\text{vib}}} - 1}, \quad (6)$$

where  $A_{\text{vib}}$  is the Einstein coefficient for the vibrational transition  $(J, v = 0) \leftrightarrow (J + 1, v = 1)$ , and  $T_0$  is the energy separation between the  $v = 1$  and  $v = 0$  levels. This process will efficiently affect the excitation of the molecule if it can populate the  $J + 2$  level before  $(J + 1, v = 1)$  decays to  $(J, v = 1)$ . In other words, following Sakamoto et al. (2010), we must have

$$P > A_{\text{rot}} \Leftrightarrow T_{\text{vib}} > T_0 / \ln(1 + A_{\text{vib}}/A_{\text{rot}}), \quad (7)$$

where  $A_{\text{rot}}$  is the Einstein coefficient for the rotational transition  $(J + 1, v = 1) \rightarrow (J, v = 1)$ . The minimum IR brightness temperature needed for the pumping to be efficient is about 100 K for the first levels of the most common dense gas tracers, such as HCN,  $\text{HCO}^+$ , and CS (e.g., Sakamoto et al. 2010).

If we compare the pumping rate with the collisional excitation rate  $C_{J-1,J} = n(\text{H}_2)q_{J-1,J}$ , we can define a pumping critical

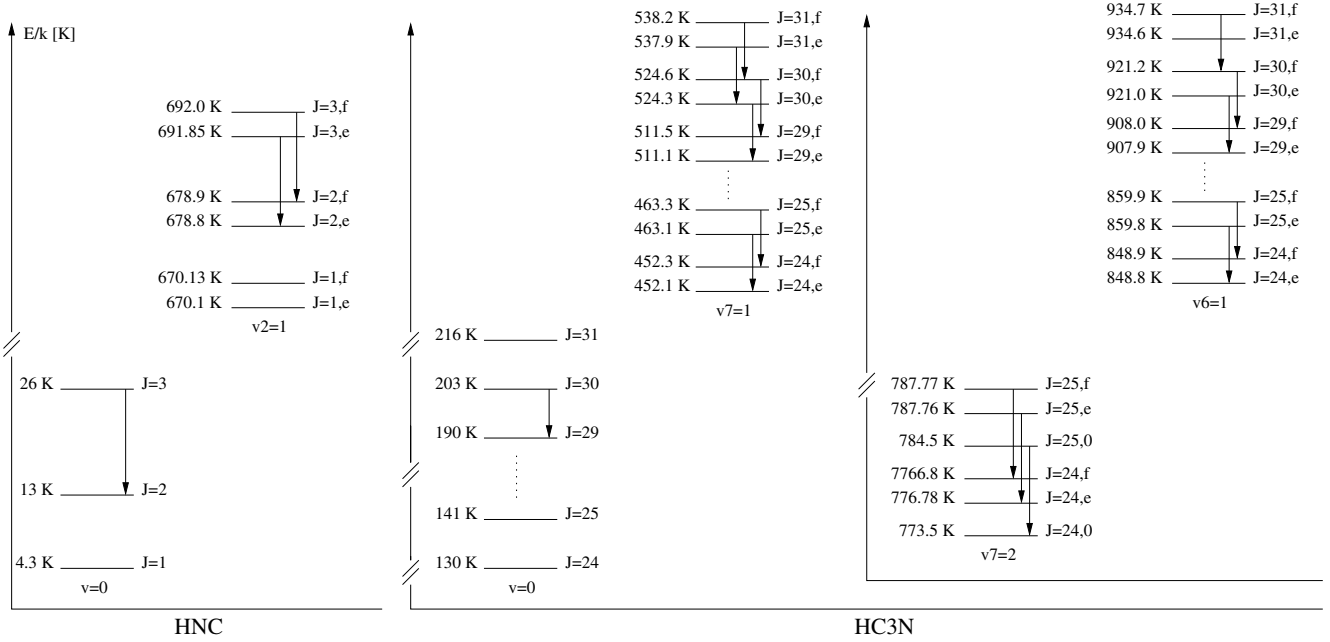


**Fig. 7.** Rotational and vibrational levels of HNC and HC<sub>3</sub>N. The solid arrows indicate the rotational transitions detected with the SMA.

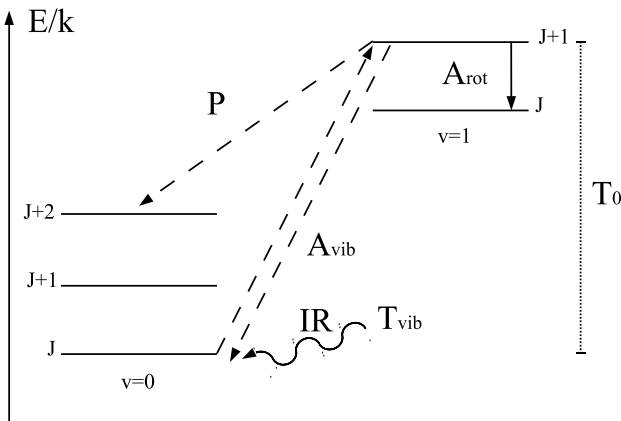


**Fig. 8.** Pumping of rotational levels via IR vibrational excitation. Rotational and vibrational transitions are drawn as solid and dashed arrows. See Sect. 4.2.2 for a discussion.

density,  $n_c = P_{\ell u}/q_{J-1,J}$ . For  $n(H_2) < n_c$  the radiative pumping process is more efficient than collisions in exciting the molecule.

In Fig. 7 we show the rotational and vibrational energy ladders for HNC and HC<sub>3</sub>N and mark the rotational transitions that we detected with the SMA. The detection of vibrationally excited HNC and HC<sub>3</sub>N allows us to estimate their vibrational temperature and directly derive the conditions for IR pumping in NGC 4418.

**HNC:** the  $v_2 = 1$  bending mode of HNC lies at 21  $\mu\text{m}$ , about 700 K above the ground state, and was first detected in space by Schilke et al. (2003) in the proto-planetary nebula CRL 618. Here we report the first (to our knowledge) extragalactic detection of mm emission from vibrationally excited HNC  $v_2 = 1$ . The intensity of the  $J = 3-2$ ,  $v_2 = 1e$  and  $v_2 = 1f$  lines, obtained from our LTE spectral fit (see Sects. 3.4.2, 4.2.1), was compared with the emission from the vibrational ground state via population-diagram analysis (see Fig. 9), which resulted in a vibrational temperature of 350 K. This value is higher than the

vibrational temperature  $\sim 230$  K found by Sakamoto et al. (2010) for HCN 4–3 in NGC 4418. This may be due to an opacity effect, since in our analysis we assumed optically thin transitions, which may not be true for the HNC,  $v = 0$  line. Moreover, because of a lower energy gap and a higher transition coefficient, the  $v_2 = 1$  vibrational state of HNC is more easily excited than the corresponding state of HCN (e.g., Aalto et al. 2007b). This could result in a larger volume of HNC to be vibrationally excited, which would show as an increase in vibrational temperature in the population diagram.

For the  $v_2 = 1$  bending mode we have  $T_0 = 669$  K, and  $A_{\text{vib}} = 5.2 \text{ s}^{-1}$  (Aalto et al. 2007b). By assuming a rotational coefficient  $A_{J=3 \rightarrow 2, v_2=1} = 8 \times 10^{-4} \text{ s}^{-1}$  (from Splatalogue) and applying Eq. (7), we find that the minimum IR brightness temperature required to efficiently pump the HNC rotational levels via the  $v_2 = 1$  vibration is 80 K. If we correctly interpret the estimated  $T_{\text{vib}}$  as a lower limit to the IR brightness temperature, it is thus possible that the molecule is being pumped. The pumping rate, estimated with Eq. (6), is  $P \approx 0.6 \text{ s}^{-1}$ . The collisional coefficients for HNC transitions can be found in the Leiden Atomic and Molecular Database<sup>7</sup> (Schöier et al. 2005). If we consider a gas kinetic temperature of 80 K (see Sect. 4.2.1), we obtain a pumping critical density of  $n_c \approx 10^9 \text{ cm}^{-3}$ .

**HC<sub>3</sub>N:** a study of vibrationally excited HC<sub>3</sub>N in NGC 4418 was first reported by Costagliola & Aalto (2010), who detected the  $v_6 = 1$  and  $v_7 = 1$  vibrationally excited states of the molecule through their rotational  $J = 10-9$ ,  $J = 17-16$ ,  $J = 25-24$  and  $J = 28-27$  mm-wave transitions. The two vibrational bending modes have IR transitions at 20 and 45  $\mu\text{m}$ , for the  $v_6 = 1$  and  $v_7 = 1$ , respectively, with critical densities  $>10^8 \text{ cm}^{-3}$ , and lie about 700 and 300 K above the vibrational ground-level.

From single-dish observations, Costagliola & Aalto (2010) found that HC<sub>3</sub>N is highly vibrationally excited, with vibrational temperatures as high as 500 K. Our population-diagram analysis confirms the high excitation, but with a lower vibrational temperature of 315 K (see Fig. 9). These two results are consistent,

<sup>7</sup> <http://www.strw.leidenuniv.nl/~moldata/>

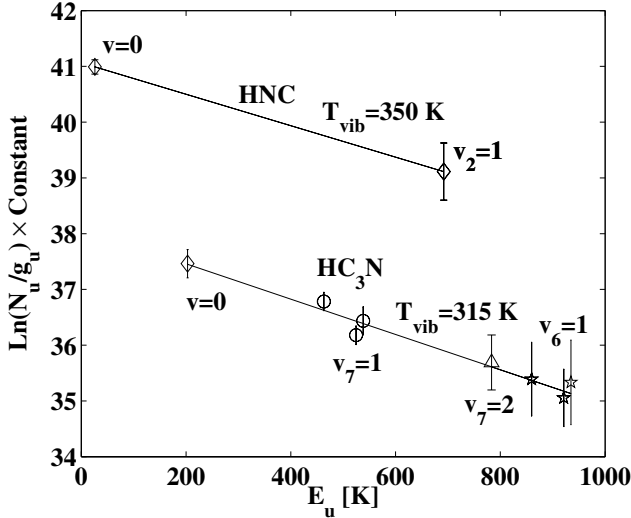


**Fig. 9.** Population diagram for vibrationally excited HNC and HC<sub>3</sub>N. For HNC, the data points relative to the  $J = 3$ ,  $v = 0$ , and  $v_2 = 1$  states are shown as open diamonds. For HC<sub>3</sub>N, the  $J = 30$ ,  $v = 0$  state is drawn as a diamond, while the  $v_6 = 1$ ,  $v_7 = 1$ , and  $v_7 = 2$  values, derived from all the observed transitions, are shown as stars, circles, and a triangle. The solid lines show the vibrational temperature fit, while error bars represent  $1\sigma$  uncertainties. For a discussion see Sect. 4.2.2.

given the large errors in the single-dish intensities derived from calibration ( $\sim 20\%$ ) and baseline instabilities. The uncertainty of our vibrational temperature measurements was calculated with a Monte Carlo method, which resulted in an estimated  $1\sigma$  error of 20%. The intensity of the tentative detection of the  $v_7 = 2$  vibrationally excited state of HC<sub>3</sub>N is also well fitted by the vibrational temperature derived for the  $v_6 = 1$  and  $v_7 = 1$  states (triangle in Fig. 9).

The vibrational coefficients are  $A_{\text{vib}} = 1.5 \times 10^{-1} \text{ s}^{-1}$  for  $v_6 = 0-1$ , and  $A_{\text{vib}} = 6 \times 10^{-4} \text{ s}^{-1}$  for  $v_7 = 0-1$  (Costagliola & Aalto 2010). The rotational coefficients for the  $J = 25-24$ ,  $J = 30-29$ , and  $J = 31-30$  are  $A_{J=25 \rightarrow 24, v=1} = 9.3 \times 10^{-4} \text{ s}^{-1}$ ,  $A_{J=30 \rightarrow 29, v=1} = 1.6 \times 10^{-3} \text{ s}^{-1}$ , and  $A_{J=31 \rightarrow 30, v=1} = 1.8 \times 10^{-3} \text{ s}^{-1}$  (from Splatalogue).

Using Eq. (7), we find that the lowest IR brightness temperature at which vibrational pumping is efficient ranges from 140 to 160 K for the  $v_6 = 1$ , and from 630 to 1100 K for the  $v_7 = 1$  transitions. Considering the estimated  $T_{\text{vib}} \approx 300 \text{ K}$ , pumping via the  $v_6 = 1$  may thus affect the molecules excitation, with a pumping rate  $P \approx 2 \times 10^{-2} \text{ s}^{-1}$ . If we assume a kinetic temperature of 80 K, the collisional coefficients for HC<sub>3</sub>N in the 1 mm band are about  $q_{J-1, J} \approx 10^{-10} \text{ cm}^3 \text{ s}^{-1}$ , which results in a critical density for IR pumping of  $n_c \approx 2 \times 10^8 \text{ cm}^{-3}$ .

In the limit of optically thin rotational emission and efficient coupling between the IR field and the molecule's vibrational modes,  $T_{\text{vib}}$  is a good estimate of the IR field temperature in the region where the lines are formed (e.g., Costagliola & Aalto 2010; Schilke et al. 2003). The fact that HNC and HC<sub>3</sub>N show similar vibrational temperatures may imply that rotational emission from the two vibrationally excited molecules is coming from a warm region, with IR temperatures of about 300 K. This is discussed in more detail in Sect. 4.5.

We found that the pumping critical densities for both HNC and HC<sub>3</sub>N have values  $n_c \geq 10^8 \text{ cm}^{-3}$ , which are higher than the typical densities found in the dense ISM. We can safely assume that only a small fraction of the gas will reside at  $n(\text{H}_2) > n_c$ ,

meaning that radiative pumping may be more efficient than collisions at populating the vibrational ground state of a detectable amount of HNC and HC<sub>3</sub>N in the nucleus of NGC 4418, or at least give a significant contribution to their excitation.

#### 4.2.3. Limitations of the LTE approach and main uncertainties

In Table 5 we report the results of our excitation analysis together with the uncertainties for the derived column densities and excitation temperatures. For molecules with only one detected transition (CO, CS, HNC ( $v = 0$ ), HC<sub>3</sub>N ( $v = 0$ )), the excitation temperature was fixed at 80 K, the peak of the CO 2–1 emission (assuming CO is optically thick). The uncertainty of 20% for the column density only accounts for the uncertainty in the data, not for the uncertainty in the excitation temperature. The fundamental assumption here is that emission from CO, CS, HNC ( $v = 0$ ), and HC<sub>3</sub>N ( $v = 0$ ) all comes from the same ISM component at 80 K, which, although likely, may not be true. For these molecules, the uncertainties on the derived column densities should therefore be interpreted as lower limits.

Our analysis assumed LTE, or at least that a single temperature can be used to describe the excitation of the molecular energy levels. For rotational transitions, this implies collisions to be dominating the excitation, which is in general true for low- $J$  transitions of most molecular tracers, which have critical densities  $n_c \leq 10^5-10^6 \text{ cm}^{-3}$ . However, because of the steep increase of  $n_c$  with  $J$ , this does not hold for the higher transitions of dense gas tracers, which could become sub-thermally excited. This could affect the column densities and temperatures derived for vibrationally excited HC<sub>3</sub>N.

However, in the presence of a strong IR field, the excitation of the high- $J$  levels is probably dominated by radiation instead of collisions, and the derived excitation temperature will reflect the radiation temperature and not the kinetic temperature of the gas. In this case, our LTE analysis would result in reasonably accurate estimates (50% uncertainty) of the column densities, and the derived excitation temperatures would be an estimate of the temperature of the IR source. This is discussed in more detail in Sect. 4.4.

In Sect. 4.2.2 we found that IR pumping could play an important role in the excitation of the rotational levels of HNC and HC<sub>3</sub>N. A non-LTE analysis, including vibrational excitation of HNC and HC<sub>3</sub>N, would be needed to quantify this effect.

#### 4.3. Comparison with Herschel observations

A thorough study of molecular absorption in NGC 4418 with the *Herschel* PACS spectrometer was performed by González-Alfonso et al. (2012). These authors found that to explain the observed absorption lines from OH, HCN, H<sub>2</sub>O and NH<sub>3</sub> a multi-component model is needed. Assuming a spherical geometry, the best fit is obtained with four different concentric components, labeled  $C_{\text{hot}}$ ,  $C_{\text{core}}$ ,  $C_{\text{warm}}$ , and  $C_{\text{ext}}$ .

The  $C_{\text{hot}}$  component is contained in the innermost 5 pc of NGC 4418 nucleus and is needed to explain the mid-IR continuum emission. It has a high temperature of 350 K, but contains only a small fraction of the total molecular mass ( $8 \times 10^3 M_{\odot}$  for a total mass of roughly  $10^8 M_{\odot}$ ).

The  $C_{\text{core}}$  and  $C_{\text{warm}}$  components extend from 5 to 30 pc, with temperatures of 150 K and 100 K, respectively. These components are needed to explain absorption from the high- and

mid-lying levels of OH, HCN, H<sub>2</sub>O, and NH<sub>3</sub> and contain most of the molecular mass, roughly  $10^8 M_{\odot}$ .

The last more extended component,  $C_{\text{ext}}$ , has a diameter of 200 pc, temperatures ranging from 30 to 90 K, and a mass of  $1.8 \times 10^7 M_{\odot}$ . This extended envelope is responsible for the observed absorption from the low-lying levels of OH and from the [O I] transition at  $63 \mu\text{m}$ , which appear redshifted from the systemic velocity of the galaxy by  $100 \text{ km s}^{-1}$ . The authors interpreted this redshifted absorbing envelope as a spherical in-flow, which would be driving molecular gas from the outer regions of NGC 4418 to its nucleus at a rate  $\leq 12 M_{\odot} \text{ yr}^{-1}$ .

The velocity and mass of our RC component, and the size of the CO 2–1 emission are consistent with the redshifted absorbing envelope proposed by [González-Alfonso et al. \(2012\)](#). The greatest uncertainty is the geometry of the in-flow. In [González-Alfonso et al. \(2012\)](#), the in-flow was modeled as a collapsing spherical shell, while we modeled the SC component as a redshifted spherical 3D Gaussian. The two different approaches may lead to differences in the estimated mass flux on the order of a few. The mass in-flow rate calculated from our CO 2–1 model is  $11\text{--}49 M_{\odot} \text{ yr}^{-1}$ , which, given the uncertainties, is consistent with what was found by *Herschel* for the in-flow envelope.

While the shell model by [González-Alfonso et al. \(2012\)](#) can explain most of the molecular absorption toward the core of NGC 4418, it overestimates the blueshifted component that one would expect in the case of a collapsing shell. Our high-resolution CO 2–1 model reveals a spatially resolved, redshifted component, displaced by  $0''.1$  from the bulk of the molecular emission, and does not show any blueshifted emission that would be compatible with a spherical in-flowing envelope. However, the SC component is still barely resolved and we need yet higher-resolution observations to determine the exact geometry of the flow.

The layered-temperature model suggested by [González-Alfonso et al. \(2012\)](#) is substantially confirmed by our interferometric observations, as discussed in the next section.

#### 4.4. Temperature structure

The LTE analysis of the detected molecular emission reveals a layered temperature structure, which most likely reflects a steep temperature gradient in the nucleus of NGC 4418. We identified three main temperature components at 80 K, 160 K, and 300 K (see Table 5 and Fig. 10).

The first component is derived from the CO 2–1 peak brightness temperature and is assumed to be associated with the spatially resolved, extended molecular material. This value is similar to the optically thick dust temperature of 85 K found by [Evans et al. \(2003\)](#) by comparing IRAS fluxes at 100 and  $60 \mu\text{m}$ , and to the temperature of the molecular gas (30–90 K) estimated by [González-Alfonso et al. \(2012\)](#) for the outer envelope in their model of *Herschel* absorption. The CO 2–1 peak is also comparable to the CO 3–2 brightness temperature reported by [Sakamoto et al. \(2013\)](#).

An intermediate temperature of 160 K derives from the rotational diagram analysis of HC<sub>3</sub>N,  $v_7 = 1$  emission. This value is consistent with what was found by [González-Alfonso et al. \(2012\)](#) for their  $C_{\text{core}}$  component (see Sect. 4.3) and with the deconvolved brightness temperature of the  $0''.1$  continuum emission at  $860 \mu\text{m}$  reported by [Sakamoto et al. \(2013\)](#).

A hot component at 300 K results both from the rotational excitation of the HC<sub>3</sub>N,  $v_6 = 1$  emission and from the vibrational

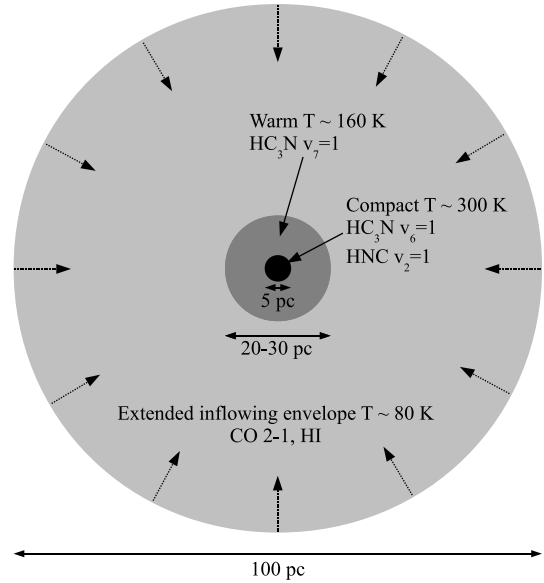


**Fig. 10.** Structure of the inner 100 pc of NGC 4418 inferred from our analysis of CO and HI dynamics and from molecular excitation. The outer envelope, traced by CO and HI, has a temperature of 80 K (from CO brightness temperature) and shows clear in-flow signatures. A warmer component, at 160 K is traced by HC<sub>3</sub>N  $v_7 = 1$  and is consistent with the 20–30 pc-wide warm component derived by [González-Alfonso et al. \(2012\)](#). A compact, 300 K component of 5 pc in diameter is traced by HC<sub>3</sub>N  $v_6 = 1$  and HNC  $v_2 = 1$ . See also Table 5.

excitation of HNC and HC<sub>3</sub>N (see Fig. 9 and Table 5). Because of their high critical densities, the IR vibrational transitions of HNC and HC<sub>3</sub>N can be excited only by radiation and provide a direct, extinction-free probe of the IR field in the inner regions of NGC 4418. Assuming an efficient coupling between IR radiation and the molecular gas, the vibrational temperature found for the two molecular species,  $T_{\text{vib}} = 315\text{--}350 \text{ K}$ , is a good estimate of the temperature of the IR emission.

The rotational temperature of HC<sub>3</sub>N,  $v_6 = 1$  ( $\sim 310 \text{ K}$ ) is remarkably similar to the IR temperature inferred from our vibrational analysis. This may imply that the vibrationally excited molecular emission is emerging from a region where the IR field and the molecular gas are at equilibrium, i.e., an IR-thick source. In their model of *Herschel* molecular absorption, [González-Alfonso et al. \(2012\)](#) needed a hot, compact ( $< 5 \text{ pc}$ ) component of  $\sim 350 \text{ K}$  to fit the observed mid-IR flux. This temperature is consistent with the hot component we detect with our excitation analysis.

In principle, the hot component does not need to be a single compact source, but any distribution of 300 K gas with a total surface area  $< (5 \text{ pc})^2$  contained in the beam would fit both SMA and *Herschel* observations. However, sub-mm observations by [Sakamoto et al. \(2013\)](#) have shown that most of the continuum dust emission is emerging from a compact region of less than  $0''.1 \approx 20 \text{ pc}$  in diameter. We can thus speculate that the mid-IR detected by *Herschel* and our vibrationally excited molecular emission are emerging from the same  $C_{\text{hot}}$ , compact region in the core of NGC 4418.

#### 4.5. What is feeding at the center of NGC 4418?

##### 4.5.1. A compact starburst?

If we assume that the entire radio flux density at 1.4 GHz is due to synchrotron emission from supernovae, following

Condon (1992) we find a supernova rate of  $0.04 \text{ yr}^{-1}$  for the inner 100 pc of NGC 4418. Assuming that all stars with mass greater than  $8 M_{\odot}$  will evolve into a supernova, the estimated supernova rate translates into a star formation rate  $SFR \approx 5 M_{\odot} \text{ yr}^{-1}$  for a Salpeter initial mass function (IMF, Salpeter 1955) between 0.1 and  $120 M_{\odot}$ , and a continuous starburst older than 30 Myr. This value is consistent with an independent estimate of the star formation rate from the far-IR luminosity. Combining IRAS observations at 60 and  $100 \mu\text{m}$ , Baan & Klöckner (2006) found an integrated (40– $120 \mu\text{m}$ ) FIR luminosity for NGC 4418 of  $\text{Log}(L_{\text{FIR}}/L_{\odot}) = 10.63$ . If we apply the prescription from Kennicutt (1998) to derive the SFR from the FIR luminosity, we find a galaxy-averaged star formation rate  $SFR \approx 7 M_{\odot} \text{ yr}^{-1}$ , which is consistent with what was derived from the radio flux. If the radio and IR luminosity is driven by star formation, this galaxy is forming more stars than the whole Milky Way in a region of only 100 pc in diameter.

In Sect. 4.1.3 we estimated for the inner 100 pc of NGC 4418 a molecular mass of  $0.6\text{--}2.5 \times 10^8 M_{\odot}$ . If we assume the mass to be uniformly distributed on a region of 100 pc in diameter, we derive a gas surface density of  $\Sigma_{\text{gas}} = 0.8\text{--}3.2 \times 10^4 M_{\odot} \text{ pc}^{-2}$ . Observations at higher spatial resolution by Sakamoto et al. (2013) showed that the bulk of the molecular gas is concentrated in a smaller region of less than 20 pc in diameter. If we assume the entire molecular gas to be contained in the inner 20 pc, the resulting surface density is  $1.9\text{--}8 \times 10^5 M_{\odot} \text{ pc}^{-2}$ . In the following discussion we adopt a conservative value of  $\Sigma_{\text{gas}} \sim 10^4 M_{\odot} \text{ pc}^{-2}$ .

Given this gas surface density, the Kennicutt-Schmidt (KS) law (e.g., Kennicutt 1998) for normal galaxies and starbursts results in a star formation rate density of  $\Sigma_{\text{SFR}} \approx 60 M_{\odot} \text{ kpc}^{-2} \text{ yr}^{-1}$ . If we assume that star formation is uniformly distributed in the central 100 pc (the extent of the 1.4 GHz continuum), the SFR derived from radio and FIR fluxes imply an observed  $\Sigma_{\text{SFR}}$  that is roughly four times higher than what is derived from the KS law. Given the uncertainties, the two values can be considered as consistent, and the high star formation rate of NGC 4418 may be just a consequence of its extreme gas surface density.

Both the radio and FIR methods discussed so far to derive the SFR assume a mature stellar population, resulting from a continuous star formation of at least 30–100 Myr. This assumption may not hold in NGC 4418, where the high luminosity-to-mass ratio together with the high obscuration suggest a much younger starburst activity. In Sakamoto et al. (2013) SMA observations at  $860 \mu\text{m}$  were used to derive a bolometric luminosity of  $10^{11} L_{\odot}$  and a ratio  $L_{\text{bol}}/M_{\text{dyn}} > 500 L_{\odot} M_{\odot}^{-1}$  for the inner 20 pc of the galaxy. These values, when compared to Starburst99 simulations (Leitherer et al. 1999), imply that if a starburst is powering the core of NGC 4418, its age must be younger than 10 Myr and must have an SFR of more than  $10 M_{\odot} \text{ yr}^{-1}$  (see Fig. 17 in Sakamoto et al. 2013).

At this rate, the total amount of molecular and neutral gas in the nucleus of NGC 4418 would be depleted in less than 30 Myr. However, we do have evidence of a molecular and atomic inflow in NGC 4418. From our dynamical model, discussed in Sect. 4.1.1, we estimated a mass flux toward the nucleus of the galaxy of  $11\text{--}49 M_{\odot} \text{ yr}^{-1}$ . Such a gas inflow could be feeding the nuclear star formation, and it would considerably lengthen the lifetime of the starburst.

The high gas surface density derived for NGC 4418 resembles the extreme values ( $\sim 5 \times 10^4 M_{\odot} \text{ pc}^{-2}$ ) found in much more massive ultra-luminous infrared galaxies (ULIRGS, e.g., Arp 220, Scoville et al. 1997). The inner 100 pc of NGC 4418 indeed share several properties with the western nucleus of the prototypical ULIRG, Arp 220. If we consider the typical radio

flux of supernova remnants (SNR) in Arp 220 (Batejat et al. 2011), the total radio emission at 1.4 GHz of NGC 4418 can be reproduced by a collection of 5 to 40 SNRs, depending on the age of the SNR. This would give a SNR surface density similar to the one observed for the western nucleus of Arp 220.

In a starburst scenario, the compact 300 K component derived from molecular vibrations could be emerging from the core of a super star cluster. To produce the observed IR luminosity, about  $10^6$  OB stars are needed (e.g., Hohle et al. 2010). These should be confined in a highly obscured region of only a few pc in size. The inferred IR luminosity and star density are higher than those commonly observed in obscured super star clusters (e.g., Sauvage & Plante 2003).

The maximum L/M before the radiation pressure on dust starts blowing away the gas of a star-forming cloud is about  $500\text{--}1000 L_{\odot} M_{\odot}^{-1}$  (e.g., Thompson et al. 2005). Our estimates of the hydrogen mass in the inner 100 pc of NGC 4418 result in an  $L/M = 500\text{--}2000 L_{\odot} M_{\odot}^{-1}$ , where the uncertainty mainly depends on the  $X_{\text{CO}}$  conversion factor (either Galactic or ULIRG, see Sect. 4.1.3). Given this large uncertainty, we cannot exclude an extreme star-cluster, emitting at the highest possible luminosity, as a possible power-source at the center of NGC 4418. We speculate that such an extreme super star cluster may be a result of the unusually high gas density in the core of NGC 4418.

The upper limit of our L/M estimate is not consistent with star formation to be powering the IR emission from the inner 100 pc. We investigate the possibility of a non-stellar contribution in the next section.

#### 4.5.2. An active galactic nucleus?

Our excitation analysis confirms the layered thermal structure suggested by González-Alfonso et al. (2012) and provides a direct detection of the hot, compact source in NGC 4418 (see Sect. 4.4). Following Evans et al. (2003), if we assume the whole IR continuum to be coming from a 300 K optically thick source, we obtain an upper limit for the size of the emitting region of just 5 pc. The existence of a compact AGN core in NGC 4418 has been proposed by several authors, mainly because of the high surface brightness in the IR (e.g., Spoon et al. 2001) and the lack of significant PAH emission in the mid-IR (Imanishi et al. 2004). The hot, compact core traced by vibrationally excited lines could be the first direct evidence of such a compact source.

Observations with the *Chandra* observatory by Maiolino et al. (2003) showed that the hard X-ray flux from NGC 4418 is very faint, consistent with a very low power, Compton-thick AGN. However, because of the poor photon statistics, the authors claimed that this interpretation has to be regarded as tentative. From our CO 2–1 observations we estimate a molecular hydrogen column in the central SMA beam of  $6 \times 10^{24} \text{ cm}^{-2}$ , which is consistent with the value of  $N(\text{H}) > 10^{25} \text{ cm}^{-2}$  derived by Sakamoto et al. (2013) for the  $0''.1$  dust continuum core. These high column densities could cause an AGN to become Compton-thick.

An empirical correlation between the bulge *K*-band luminosity and black hole mass has been found both for Seyfert and normal galaxies (e.g., Peng et al. 2006). An estimate of the mass of a supermassive black hole in the center of NGC 4418 can therefore be obtained from observations in the *K* band. The total *K*-band luminosity observed by the 2MASS mission (Skrutskie et al. 2006) is  $L_{\text{K}} \approx 2 \times 10^{10} L_{\odot}$ . This corresponds to a black hole mass of roughly  $M_{\text{BH}} \approx 7 \times 10^6 M_{\odot}$  (see Fig. 4 in Peng et al. 2006). As discussed in Sakamoto et al. (2013), the luminosity-to-mass ratio observed for the nucleus of NGC 4418 could be

reproduced by an AGN of  $1 \times 10^7 M_{\odot}$ , radiating at 30% of its Eddington limit.

For radio-quiet AGNs, Nelson (2000) found that the radio power and black hole mass are correlated. According to their Fig. 2, a black hole with a mass of  $7 \times 10^6 M_{\odot}$  should have a radio luminosity at 1.4 GHz of  $3 \times 10^{21} \text{ W Hz}^{-1}$ , which is roughly ten times higher than the total radio luminosity observed for NGC 4418. For some reason, if an AGN is present in the center of the galaxy, it should be radio deficient. However, the empirical correlations just mentioned have quite a large scatter (especially the  $L_K/M_{\text{BH}}$  relation) and their theoretical interpretation is still debated. It is also possible that the radio emission is being affected by synchrotron self-absorption or free-free absorption.

The low  $\text{HCO}^+/\text{HCN } J = 1-0$  line ratio observed in NGC 4418 has been interpreted by some authors as a signature of AGN activity (e.g., Kohno et al. 2001; Krips et al. 2008). Standard models of X-ray-dominated chemistry (e.g., Meijerink et al. 2007), which should be dominant in an AGN environment, show instead an enhancement of  $\text{HCO}^+$  emission due to the high ionization, and consequently a high  $\text{HCO}^+/\text{HCN}$  ratio. Moreover, the presence of bright  $\text{HC}_3\text{N}$  emission is difficult to explain in an AGN scenario, because the molecule is easily destroyed by reactions with atomic and molecular ions and by UV radiation (e.g., Turner et al. 1998). In a high-resolution study of the chemistry of IC 342, Meier & Turner (2005) indeed found that  $\text{HC}_3\text{N}$  emission follows the 3 mm continuum dust emission, and anti-correlates with regions of intense UV radiation, such as photo-dissociation regions (PDRs). However, recent models by Harada et al. (2010), show that high-temperature reactions ( $T > 400 \text{ K}$ ) can enhance  $\text{HC}_3\text{N}$  abundances on the plane of a dense AGN accretion torus. The bright emission from vibrationally excited  $\text{HC}_3\text{N}$  may therefore be coming from a small region in the accretion disk. Models show that the size of such a region probably is a few pc, which would be consistent with what we estimate from  $\text{HC}_3\text{N}$  and  $\text{HCN}$  vibrational temperatures.

## 5. Conclusions

We have observed the compact obscured nucleus of NGC 4418 with MERLIN and the SMA at radio and mm wavelengths. The radio emission at 1.4 and 5 GHz is spatially resolved, with an estimated source size of 80 and 25 pc. The CO 2–1 emission and HI absorption were fit by a two-component model with the two Gaussian components, and have centroid velocities of 2090 and 2180  $\text{km s}^{-1}$  and hydrogen masses of  $0.6\text{--}2.5 \times 10^8$  and  $1.1\text{--}4.3 \times 10^7 M_{\odot}$ . These observations confirm the existence of inflowing gas toward the nucleus of NGC 4418, which was first detected in absorption by González-Alfonso et al. (2012) with *Herschel*. We estimated the molecular and atomic in-flow to be feeding the central activity at a rate of  $11\text{--}49 M_{\odot} \text{ yr}^{-1}$ .

Vibrationally excited  $\text{HC}_3\text{N}$  and  $\text{HNC}$  were detected with vibrational temperatures of roughly 300 K. The molecular excitation in NGC 4418 is consistent with a layered temperature structure, with three main components at 80, 160, and 300 K. These probably reflect a steep temperature gradient and not three distinct temperatures. For the hot component we estimated a source size of less than 5 pc. We discussed the radiative pumping of the  $\text{HC}_3\text{N}$  and  $\text{HNC}$  rotational levels via vibrational transitions and found that this may play an important role in the excitation of the molecules.

If the radio and FIR emission is produced by star formation, the high  $L/M$  ratio implies a star formation rate of  $\sim 10 M_{\odot} \text{ yr}^{-1}$  and a starburst age younger than 10 Myr. In contrast, the radio continuum may be emerging from an AGN. Using an empirical

relation between the black hole mass and  $K$ -band luminosity, we estimated  $M_{\text{BH}} \approx 7 \times 10^6 M_{\odot}$  for the putative black hole in the center of NGC 4418. The total 1.4 GHz flux density derived from MERLIN observations is roughly ten times lower than what would be expected for an AGN of this mass.

Despite these high angular resolution observations, the nature of the central energy source in NGC 4418 is still unclear. However, this study provides some new constraints on the properties of the nuclear starburst or AGN:

- If a compact starburst is producing the observed IR luminosity, it has to be at least as extreme as the one observed in Arp 220. If we consider the estimated gas depletion time of 30 Myr and the high  $L/M > 500 L_{\odot} M_{\odot}^{-1}$ , the starburst must be 3 to 10 Myr old.
- If an AGN is feeding at the center of NGC 4418, it must be Compton-thick, so that its presence is not clearly revealed by hard X-rays observations. The low radio flux observed may either be due to an intrinsic property of the AGN or to highly compact free-free absorption.

Wide-field VLA observations suggest that NGC 4418 is capturing gas from its HI-rich companion (Klöckner et al., in prep.). This gas appears to be entering NGC 4418 from the northeastern side of the galaxy. How the captured gas moves from the 16 kpc-scale atomic bridge into the inner 100 pc of NGC 4418 is unclear.

The compactness of NGC 4418 nucleus appears to be the key to the observed extreme properties of gas and dust. Similar gas properties are observed in ULIRGs such as Arp 220, but these are usually interacting systems of much larger mass.

*Acknowledgements.* F.C. acknowledges support by the Spanish MINECO through grant AYA 2012-38491-C02-02, co-funded with FEDER funds.

## References

- Aalto, S., Monje, R., & Martín, S. 2007a, A&A, 475, 479  
Aalto, S., Spaans, M., Wiedner, M. C., & Hüttemeister, S. 2007b, A&A, 464, 193  
Baan, W. A., & Klöckner, H.-R. 2006, A&A, 449, 559  
Baan, W. A., Henkel, C., Loenen, A. F., Baudry, A., & Wiklind, T. 2008, A&A, 477, 747  
Batejat, F., Conway, J. E., Hurley, R., et al. 2011, ApJ, 740, 95  
Carroll, T. J., & Goldsmith, P. F. 1981, ApJ, 245, 891  
Condon, J. J. 1992, ARA&A, 30, 575  
Costagliola, F., & Aalto, S. 2010, A&A, 515, A71  
Costagliola, F., Aalto, S., Rodríguez, M. I., et al. 2011, A&A, 528, A30  
Elmegreen, B. G., & Efremov, Y. N. 1997, ApJ, 480, 235  
Evans, A. S., Becklin, E. E., Scoville, N. Z., et al. 2003, AJ, 125, 2341  
Goldsmith, P. F., & Langer, W. D. 1999, ApJ, 517, 209  
González-Alfonso, E., Fischer, J., Graciá-Carpio, J., et al. 2012, A&A, 541, A4  
Harada, N., Herbst, E., & Wakelam, V. 2010, ApJ, 721, 1570  
Hohle, M. M., Neuhäuser, R., & Schutz, B. F. 2010, Astron. Nachr., 331, 349  
Imanishi, M., Nakanishi, K., Kuno, N., & Kohno, K. 2004, AJ, 128, 2037  
Kennicutt, Jr., R. C. 1998, ARA&A, 36, 189  
Kohno, K., Matsushita, S., Vila-Vilaró, B., et al. 2001, in The Central Kiloparsec of Starbursts and AGN: The La Palma Connection, eds. J. H. Knapen, J. E. Beckman, I. Shlosman, & T. J. Mahoney, ASP Conf. Ser., 249, 672  
Krips, M., Neri, R., García-Burillo, S., et al. 2008, ApJ, 677, 262  
Leitherer, C., Schaerer, D., Goldader, J. D., et al. 1999, ApJS, 123, 3  
Maiolino, R., Comastri, A., Gilli, R., et al. 2003, MNRAS, 344, L59  
Martín, S., Krips, M., Martín-Pintado, J., et al. 2011, A&A, 527, A36  
Meier, D. S., & Turner, J. L. 2005, ApJ, 618, 259  
Meijerink, R., Spaans, M., & Israel, F. P. 2007, A&A, 461, 793  
Müller, H. S. P., Schlöder, F., Stutzki, J., & Winnewisser, G. 2005, J. Mol. Struct., 742, 215  
Nelson, C. H. 2000, ApJ, 544, L91  
Papadopoulos, P. P., van der Werf, P., Xilouris, E., Isaak, K. G., & Gao, Y. 2012, ApJ, 751, 10

- Peng, Z., Gu, Q., Melnick, J., & Zhao, Y. 2006, *A&A*, 453, 863
- Pérez-Torres, M. A., Romero-Cañizales, C., Alberdi, A., & Polatidis, A. 2009, *A&A*, 507, L17
- Pickett, H. M., Poynter, R. L., Cohen, E. A., et al. 1998, *J. Quant. Spec. Radiat. Transf.*, 60, 883
- Roche, P. F., Aitken, D. K., Smith, C. H., & James, S. D. 1986, *MNRAS*, 218, 19P
- Rohlfs, K., & Wilson, T. L. 1996, *Tools of Radio Astronomy* (Berlin, New York: Springer)
- Roussel, H., Helou, G., Beck, R., et al. 2003, *ApJ*, 593, 733
- Sakamoto, K., Aalto, S., Evans, A. S., Wiedner, M. C., & Wilner, D. J. 2010, *ApJ*, 725, L228
- Sakamoto, K., Aalto, S., Costagliola, F., et al. 2013, *ApJ*, 764, 42
- Salpeter, E. E. 1955, *ApJ*, 121, 161
- Sanders, D. B., & Mirabel, I. F. 1996, *ARA&A*, 34, 749
- Sanders, D. B., Mazzarella, J. M., Kim, D.-C., Surace, J. A., & Soifer, B. T. 2003, *AJ*, 126, 1607
- Sauvage, M., & Plante, S. 2003, *Ap&SS*, 284, 941
- Schilke, P., Walmsley, C. M., Pineau Des Forets, G., et al. 1992, *A&A*, 256, 595
- Schilke, P., Comito, C., & Thorwirth, S. 2003, *ApJ*, 582, L101
- Schöier, F. L., van der Tak, F. F. S., van Dishoeck, E. F., & Black, J. H. 2005, *A&A*, 432, 369
- Scoville, N. Z., Yun, M. S., & Bryant, P. M. 1997, *ApJ*, 484, 702
- Skrutskie, M. F., Cutri, R. M., Stiening, R., et al. 2006, *AJ*, 131, 1163
- Solomon, P. M., Downes, D., Radford, S. J. E., & Barrett, J. W. 1997, *ApJ*, 478, 144
- Spaans, M., & Meijerink, R. 2004, *Ap&SS*, 295, 239
- Spoon, H. W. W., Keane, J. V., Tielens, A. G. G. M., Lutz, D., & Moorwood, A. F. M. 2001, *A&A*, 365, L353
- Spoon, H. W. W., Marshall, J. A., Houck, J. R., et al. 2007, *ApJ*, 654, L49
- Swinbank, A. M., Papadopoulos, P. P., Cox, P., et al. 2011, *ApJ*, 742, 11
- Thompson, T. A., Quataert, E., & Murray, N. 2005, *ApJ*, 630, 167
- Turner, B. E., Lee, H., & Herbst, E. 1998, *ApJS*, 115, 91
- Wyrowski, F., Schilke, P., & Walmsley, C. M. 1999, *A&A*, 341, 882
- Yamada, K. M. T., & Creswell, R. A. 1986, *J. Mol. Spectr.*, 116, 384
- Yao, L., Seaquist, E. R., Kuno, N., & Dunne, L. 2003, *ApJ*, 588, 771

## Appendix A: Visibility fits

To derive source sizes for the observed emission, a simple model of a point source and a circular Gaussian was fit to the circle-averaged visibilities. These were derived by an azimuthal average around the  $u-v$  plane center with the UV\_CIRCLE routine of the MAPPING software. Averaged visibilities are plotted in Fig. A.1. On the  $x$ -axis we show the distance from the  $u-v$  center  $\sqrt{u^2 + v^2}$  in meters. The fitted parameters for the point source and Gaussian components are labeled *PS* and *RS*, respectively.

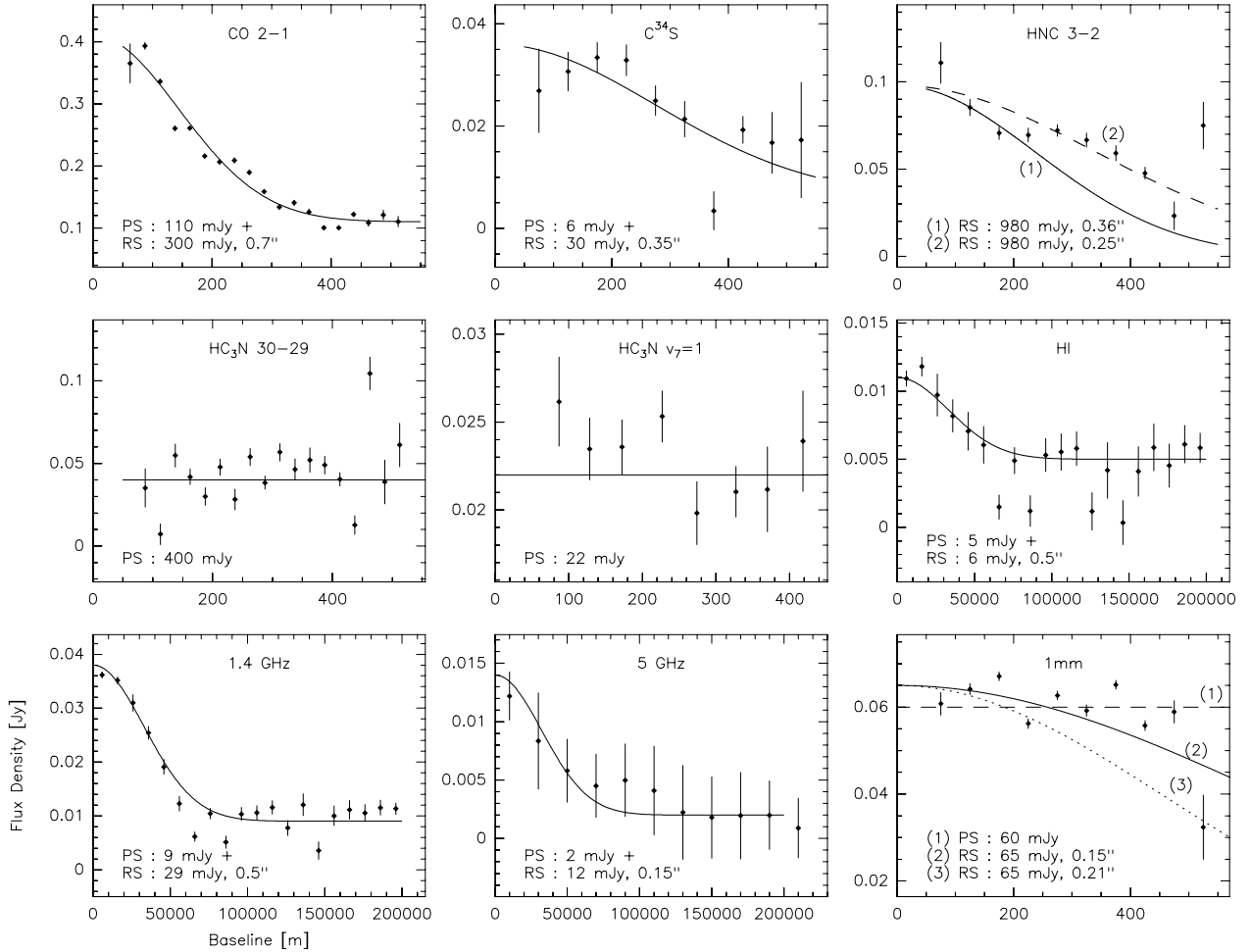


**Fig. A.1.** Circle-averaged visibility fits. The best-fit parameters are labeled PS for the point source component and RS for the resolved component. The FWHM of the resolved component is given in arcseconds. For HNC and the continuum at 1 mm, the averaged visibilities are compared with models of different source size, which are labeled as (1)...(3).